

See discussions, stats, and author profiles for this publication at: <https://www.researchgate.net/publication/340856277>

A fundamental theorem for eco-environmental surface modelling and its applications

Article in *Science China Earth Sciences* · April 2020

DOI: 10.1007/s11430-019-9594-3

CITATIONS
33

READS
579

40 authors, including:



Tian-Xiang Yue
Chinese Academy of Sciences
118 PUBLICATIONS 1,861 CITATIONS

[SEE PROFILE](#)



Yu Liu
Shandong University of Science and Technology
15 PUBLICATIONS 230 CITATIONS

[SEE PROFILE](#)



Yifu Wang
Beijing Forestry University
19 PUBLICATIONS 255 CITATIONS

[SEE PROFILE](#)



Zemeng Fan
Chinese Academy of Sciences
59 PUBLICATIONS 663 CITATIONS

[SEE PROFILE](#)

Some of the authors of this publication are also working on these related projects:



Ecological simulation [View project](#)



Mississauga Evacuation [View project](#)

A fundamental theorem for eco-environmental surface modelling and its applications

Tianxiang YUE^{1,2,3,22*}, Na ZHAO^{1,2,22}, Yu LIU⁴, Yifu WANG⁵, Bin ZHANG⁶, Zhengping DU¹, Zemeng FAN^{1,2,22†}, Wenjiao SHI^{1,2}, Chuanfa CHEN⁴, Mingwei ZHAO⁷, Dunjiang SONG⁸, Shihai WANG¹, Yinjun SONG¹, Changqing YAN⁹, Qiquan LI¹⁰, Xiaofang SUN¹¹, Lili ZHANG¹², Yongzhong TIAN¹³, Wei WANG¹⁴, Ying'an WANG¹⁵, Shengnan MA¹⁶, Hongsheng HUANG³, Yimin LU¹⁷, Qing WANG¹⁸, Chenliang WANG¹, Yuzhu WANG¹⁹, Ming LU²⁰, Wei ZHOU^{1,13,21}, Yi LIU^{1,2}, Xiaoze YIN¹, Zong WANG^{1,2}, Zhengyi BAO^{1,2}, Miaomiao ZHAO^{1,2}, Yapeng ZHAO^{1,2}, Yimeng JIAO^{1,2}, Ufra NASEER^{1,2}, Bin FAN^{1,2}, Saibo LI^{1,2}, Yang YANG^{1,2} & John P. WILSON^{1,2,23}

¹ State Key Laboratory of Resources and Environment Information System, Institute of Geographical Sciences and Natural Resources Research, Chinese Academy of Sciences, Beijing 100101, China;

² College of Resources and Environment, University of Chinese Academy of Sciences, Beijing 100049, China;

³ College of Land Resources and Environment, Jiangxi Agricultural University, Nanchang 330045, China;

⁴ College of Geomatics, Shandong University of Science and Technology, Qingdao 266590, China;

⁵ College of Forestry, Beijing Forestry University, Beijing 100083, China;

⁶ School of Land and Resources, China West Normal University, Nanchong 637002, China;

⁷ College of Geographical Information and Tourism, Chuzhou University, Chuzhou 239000, China;

⁸ Institutes of Science and Development, Chinese Academy of Sciences, Beijing 100190, China;

⁹ Department of Information Engineering, Shandong University of Science and Technology, Tai'an 271019, China;

¹⁰ College of Resources, Sichuan Agricultural University, Chengdu 611130, China;

¹¹ College of Geography and Tourism, Qufu Normal University, Rizhao 276828, China;

¹² Aerospace Information Research Institute, Chinese Academy of Sciences, Beijing 100101, China;

¹³ School of Geographical Science, Southwest University, Chongqing 400715, China;

¹⁴ National Disaster Reduction Center of China, Ministry of Emergency Management, Beijing 100721, China;

¹⁵ Department for Population Data, China Population and Development Research Center, Beijing 100081, China;

¹⁶ Department for Industrial Standard, China Standardization Administration, Beijing 100088, China;

¹⁷ The Academy of Digital China, Fuzhou University, Fuzhou 350002, China;

¹⁸ National Institute of Environmental Health, Chinese Center for Disease Control and Prevention, Beijing 100021, China;

¹⁹ School of Information Engineering, China University of Geoscience, Beijing 100083, China;

²⁰ Qian Xuesen Laboratory of Space Technology, Beijing 100094, China;

²¹ College of Architecture and Urban Planning, Chongqing Jiaotong University, Chongqing 400074, China;

²² Jiangsu Center for Collaborative Innovation in Geographical Information Resource Development and Application, Nanjing 210023, China;

²³ Spatial Sciences Institute, University of Southern California, Los Angeles, CA 90089-0374, USA

Received July 28, 2019; revised February 4, 2020; accepted February 25, 2020; published online April 21, 2020

* Corresponding author (email: yue@lreis.ac.cn)

† Corresponding author (email: fanzm@lreis.ac.cn)

Abstract We propose a fundamental theorem for eco-environmental surface modelling (FTEEM) in order to apply it into the fields of ecology and environmental science more easily after the fundamental theorem for Earth's surface system modeling (FTESM). The Beijing-Tianjin-Hebei (BTH) region is taken as a case area to conduct empirical studies of algorithms for spatial upscaling, spatial downscaling, spatial interpolation, data fusion and model-data assimilation, which are based on high accuracy surface modelling (HASM), corresponding with corollaries of FTEEM. The case studies demonstrate how eco-environmental surface modelling is substantially improved when both extrinsic and intrinsic information are used along with an appropriate method of HASM. Compared with classic algorithms, the HASM-based algorithm for spatial upscaling reduced the root-mean-square error of the BTH elevation surface by 9 m. The HASM-based algorithm for spatial downscaling reduced the relative error of future scenarios of annual mean temperature by 16%. The HASM-based algorithm for spatial interpolation reduced the relative error of change trend of annual mean precipitation by 0.2%. The HASM-based algorithm for data fusion reduced the relative error of change trend of annual mean temperature by 70%. The HASM-based algorithm for model-data assimilation reduced the relative error of carbon stocks by 40%. We propose five theoretical challenges and three application problems of HASM that need to be addressed to improve FTEEM.

Keywords HASM, FTEEM, Spatial upscaling, Spatial downscaling, Spatial interpolation, Data fusion, Model-data assimilation, Model coupling

Citation: Yue T, Zhao N, Liu Y, Wang Y, Zhang B, Du Z, Fan Z, Shi W, Chen C, Zhao M, Song D, Wang S, Song Y, Yan C, Li Q, Sun X, Zhang L, Tian Y, Wang W, Wang Y, Ma S, Huang H, Lu Y, Wang Q, Wang C, Wang Y, Lu M, Zhou W, Liu Y, Yin X, Wang Z, Bao Z, Zhao M, Zhao Y, Jiao Y, Naseer U, Fan B, Li S, Yang Y, Wilson J P. 2020. A fundamental theorem for eco-environmental surface modelling and its applications. *Science China Earth Sciences*, 63, <https://doi.org/10.1007/s11430-019-9594-3>

1. Introduction

1.1 The classic methods for surface modelling

A raster expression of a region or one of its eco-environmental properties can be abstracted to a mathematical surface (Yue et al., 2007). Various methods have been developed for surface modelling since the 1950s. Krige (1951), for example, proposed the basic idea of what today is the Kriging suite of geostatistical methods, which considers position relations between given rasters and ones to be estimated as well as spatial relations among variables. The Kriging method is a linear least squares regression. Birkhoff and Garabedian (1960) expanded the spline approximation, which had been developed by Schoenberg in 1946, to a spline function in two dimensions. De Boor (1962) successfully constructed a bicubic spline function using a two-dimension mesh. Bengtsson and Nordbeck (1964) established an irregular triangular network (TIN) for creating a surface by using irregularly distributed point data. Zienkiewicz (1967) proposed a finite element method. Akima (1978a, 1978b) completed the computer programming of the finite element method (FEM) for fitting a surface. Shepard (1968) published the method for inverse distance weighting (IDW), for which the results are closely related to the selected weight (Franke, 1982). Harder and Desmarais (1972) proposed an interpolation method using splines, which is based on the infinite plate deflection equation. Maude (1973) proposed a Rectangle Based Blending method that generalized the idea of quintic splines to several variables. Talmi and Gilat (1977) constructed a method for smooth approximation of data based on the Spline idea, which had many advantages compared with polynomial interpolation. Foley and Nielson (1980) proposed an iteration method for producing a surface

approximation, which is based on Bernstein's polynomial and bicubic spline.

Since the 1980s, methods for surface modeling have been extensively used to analyze and understand the spatial aspects of ecological and environmental processes, for which errors are a big challenge. For example, IDW fails to incorporate the spatial structure and ignores information beyond the neighborhood because an inverse distance weighting function is used to determine the interpolation value for any given point within the calculated area (Zhao et al., 2005; Magnusson et al., 2007). TINs ignore non-linear information and are unable to represent cliffs, caves or holes because the value of each point within a triangle is calculated by a linear function based on its location (Tse and Gold, 2004; Schneider, 2001). The goals of Kriging are practically unattainable since the mean error and the variance of the errors are always unknown. This suite of methods generate mean residuals or errors equal to zero by minimizing the variance of the errors (Isaks and Srivastava, 1989). Few types of surfaces fit the formulation of univariate cubic basis splines (Yue, 2011).

Uncertainty and scale issues have been high priority research topics in geographic information science (Zhu, 2005; Li, 2007). In 1983, the U.S. National Aeronautics and Space Administration brought leading scientists together to discuss uncertainty and scale issues along with other research priorities for advancing geographic information systems. In 1994, the University Consortium for Geographical Information Science (UCGIS) was founded to support academic research and teaching and in 1996, it produced a series of white papers, including one on uncertainty and scale issues, to delineate research priorities. In 2003, the UCGIS included the uncertainty and scale issues as long-term chal-

lenges in the formal UCGIS research agenda (Usery and McMaster, 2005).

1.2 The fundamental theorem for eco-environmental surface modelling

The mathematical surface is uniquely defined by the intrinsic and extrinsic properties in terms of the fundamental theorem of surfaces (FTS) (Somasundaram, 2005). The intrinsic properties can be gathered from local information, which might come from detailed ground observations. The extrinsic properties can be gathered from global information, including satellite observations and the simulation results of spatial models on large scales. The urgency and necessity of integrating the extrinsic and intrinsic properties have been discussed at various scales (Phillips, 2002; Seppelt et al., 2013; Yue et al., 2015a, 2016a). Surface modelling is a process of constructing a surface model for dynamically describing an Earth's surface system (ESS) or a specific component of the Earth's surface environment (Yue, 2011).

A method for high accuracy surface modeling (HASM) has been developed since 1986 (Yue and Ai, 1990; Yue et al., 2007, 2015b) to integrate the extrinsic and intrinsic properties and find solutions for the error and multi-scale problems that are prevalent when each type of information is used separately (Appendix 1, <https://link.springer.com>). The development of HASM can be divided into 4 stages. In the first stage from 1986 to 2001, a surface was regarded as a combination of its profiles that were fitted in terms of the fundamental theorem for curves (FTC). It was learnt that slope and curvature are significant variables of surface analysis (Evans, 1980). In fact, a profile of the Earth's surface is uniquely determined by its elevation, slope and curvature in terms of the curve-theorem in the plane (Spivak, 1979). A model was constructed for a cirque surface in terms of the FTC (Yue and Ai, 1990) and was then used for environmental change detection (Yue et al., 2002).

However, the modeling of the Earth's surface should be based on FTS instead of FTC. It has been shown that the equation of the Earth's surface can be formulated as $z=f(x, y)$, where z is an attribute value of the Earth's surface at location (x, y) (Kerimov, 2009). For the surface, a master equation set of HASM was constructed in terms of FTS (Yue et al., 2004, 2007, 2010a), which was transformed into a symmetric positive-definite and large sparse linear system. In this second stage from 2001 to 2007, we found solutions for error and multi-scale problems that plagued surface modelling prior to the development of HASM.

Although the error and multi-scale problems were solved during the second stage, HASM could only be used with small areas because it must use the master equation set for simulating each lattice of a surface, which incurs a huge computation cost. To speed up the computation of HASM,

we developed a multi-grid method of HASM (HASM-MG) (Yue and Song, 2008; Yue et al., 2013a), an adaptive method of HASM (HASM-AM) (Yue et al., 2010a), an adjustment computation of HASM (HASM-AC) (Yue and Wang, 2010), and a preconditioned conjugate gradient algorithm of HASM (HASM-PCG) (Yue et al., 2010b). In this third stage from 2008 to 2011, we solved the low computational speed and large memory requirement problems.

HASM was successfully applied for constructing digital terrain models (Chen and Yue, 2010; Chen et al., 2013a, 2013b), filling voids in the Shuttle Radar Topography Mission (SRTM) dataset (Yue et al., 2012), simulating climate change (Yue et al., 2013b, 2016b; Zhao and Yue, 2014a, 2014b; Zhao et al., 2018), estimating carbon stocks (Yue et al., 2016c), fusing satellite observations and the Total Carbon Column Observing Network (TCCON) measurements of the column-averaged dry air mole fraction of CO₂ (XCO₂) (Zhang et al., 2017a; Zhao et al., 2017), filling voids on remotely sensed XCO₂ surfaces (Yue et al., 2015b), modeling surface soil properties (Shi et al., 2011) and soil pollution (Shi et al., 2009), and analyzing ecosystem responses to climatic change (Yue et al., 2015c). In all of these applications, HASM produced more accurate results than the classical methods.

During the fourth stage from 2011 to 2016, the fundamental theorem for earth surface system modeling (FTESM) was proposed on the basis of developing the HASM methods and their successful applications. FTESM is based on a combination of surface theory, system theory, and optimal control theory (Somasundaram, 2005; Djaferis and Schick, 2000; Hull, 2003). The FTESM can be summarized as follows: an Earth's surface system or a component of the Earth's surface environment, is uniquely defined by both extrinsic and intrinsic properties of the surface, which can be simulated with an appropriate method for integrating the extrinsic and intrinsic properties, such as HASM, when the spatial resolution of the surface is sufficient to capture the attribute(s) of interest (Yue et al., 2016a). In other words, accurate modeling of the Earth's surface systems requires both extrinsic and intrinsic information as well as appropriate methods.

If an eco-environmental surface is, as a unified term, used to represent a surface of nature, a surface of nature's contribution and a surface of a driving-force of natural changes, a fundamental theorem for eco-environmental surface modelling (FTEEM) can be created after the FTESM (IPBES, 2016, 2019). The FTEEM can be stated as follows: an eco-environmental surface is uniquely defined by both extrinsic information and intrinsic information of the surface, which can be simulated with an appropriate method for integrating the global and local information, such as HASM, when the spatial resolution of the surface is fine enough to capture the attribute(s) of interest.

In this paper, we take the Beijing-Tianjin-Hebei (BTH) region as a case study area to demonstrate that both extrinsic and intrinsic information as well as an appropriate method for integrating these information streams are essential for eco-environmental surface modelling with high accuracy. The BTH region that consists of Beijing municipality, Tianjin municipality, and Hebei province, is located in between latitude $35^{\circ}03'N$ - $42^{\circ}40'N$ and longitude $113^{\circ}27'E$ - $119^{\circ}50'E$ (Figure 1). The BTH region, which is located in north China and surrounded by the Yanshan and Taihang mountains and Bohai Sea, covers an area of 217800 km^2 . The region was home to 112.47 million residents in 2017, about 8.1% of China's total population (National Bureau of Statistics of China, 2018).

Following the release of the plan for the Coordinated Development for the Beijing-Tianjin-Hebei Region (CDBTH) by the central government of China in April 2015, the focus has shifted to development-oriented solutions for ecological, social, and economic problems as well as the incorporation of considerations of environmental sustainability in development planning. This focus places a premium on understanding spatiotemporal dynamics across multiple spatial and temporal scales and as we show below, this need motivated the work at hand.

2. Spatial upscaling of the elevation surface

Upscaling refers to the transfer of knowledge from a finer to a coarser resolution in order to reduce computational costs

(Misaghian et al., 2018). Upscaling via simple spatial averaging frequently results in unacceptable errors (Crow et al., 2012; Fry et al., 2017).

We upscale the elevation surface of the BTH region from a spatial resolution of 90 to 1000 m by combining data from the Shuttle Radar Topography Mission (SRTM) ([http://srtm.cgiar.org/](http://srtm.csi.cgiar.org/)) with ground observations using global positioning system (GPS) based on continuously operating reference stations (CORS)

A spatial upscaling algorithm was developed using HASM, which is termed HASM-US (Appendix 2). HASM-US uses both intrinsic and extrinsic information as well as the appropriate method, HASM, for integrating them. A total of 560 points with information on altitude and geographic coordinates (Figure 2), observed using GPS-based from CORS, was divided into 10 data sets. Nine data sets were employed as the optimal control constraints of HASM-US and the remaining data set was used for cross-validation. The maximum positive absolute error (MPAE), maximum negative absolute error (MNAE) and root-mean-square error (RMSE) of HASM-US were calculated and compared with the same metrics of two widely used upscaling algorithms, bilinear resampling (BR) and adjacent point resampling (ARP).

The cross-validation results indicated that the MPAE, MNAE and RMSE of HASM-US are 59, -70 and 19 m, respectively, whereas those for BR are 72, -107 and 28 m and those for ARP are 77, -113 and 28 m, respectively (Table 1). The maximum amplitudes of HASM-US, BR and ARP are 129, 179 and 190 m, respectively and taken as a

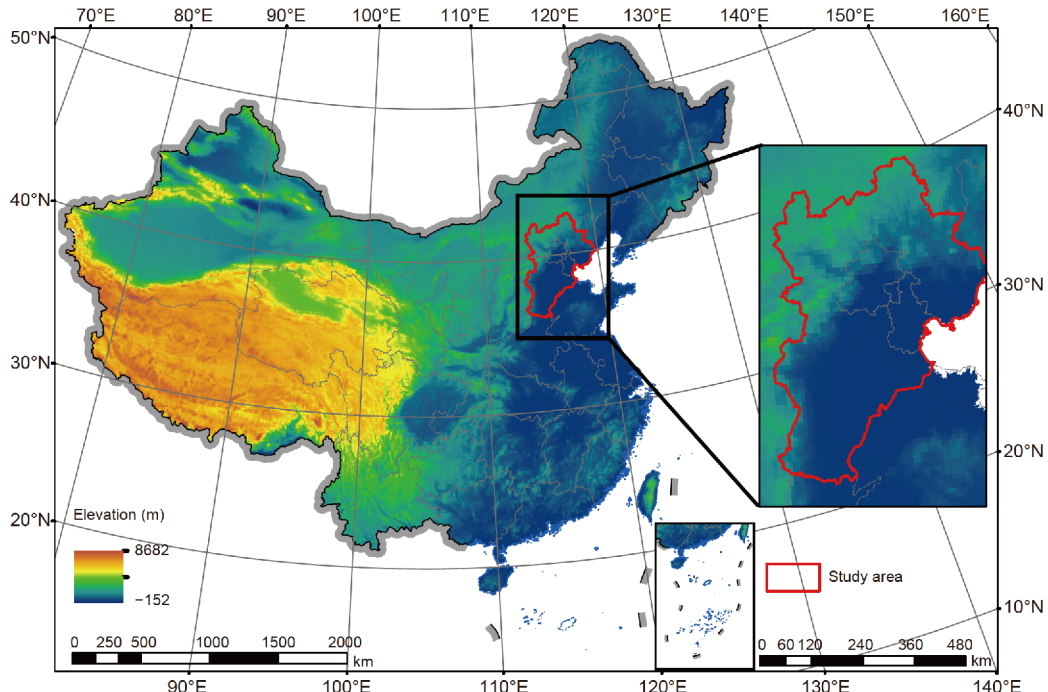


Figure 1 Location of Beijing-Tianjin-Hebei region.

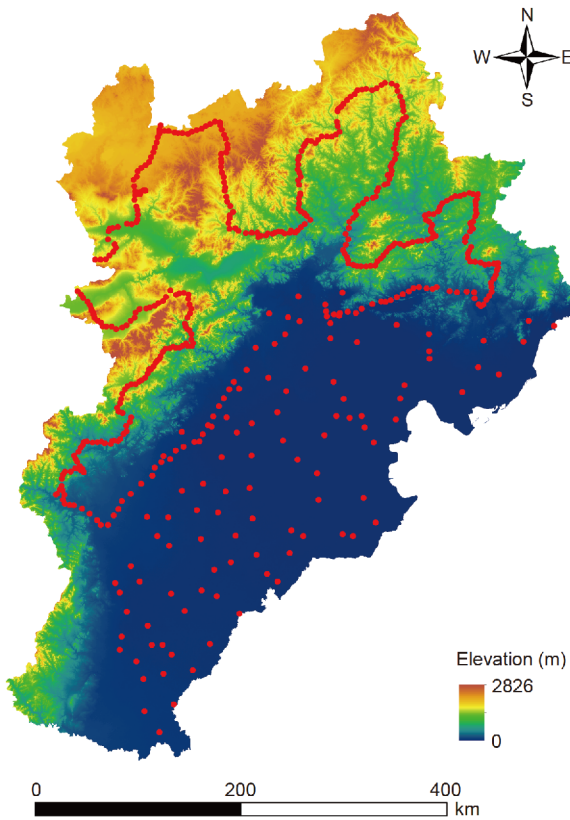


Figure 2 Sample points of elevation using GPS-based from CORS.

whole, the aforementioned metrics indicate that HASM-US has the highest accuracy and the most stable performance of the three methods considered.

In terms of HASM-US, the BTH region is divided into two sub-regions using 1000 m as the cutoff. The lower-elevation sub-region accounts for 77.46% of BTH, about 166698 km²; and the middle-elevation sub-region accounts for 22.54%, or about 48510 km². The lower-elevation sub-region is classi-

fied into six steps and the middle-elevation sub-region with a highest altitude of 2824 m is classified into five steps (Figure 3; Table 2). The first step accounting for 48.39% of BTH region, lower than 50 m, dominates the lower-elevation sub-region and the eighth step accounting for 51.48% of BTH region, between 1200 and 1500 m, stands out in the middle-elevation sub-region.

Relief amplitude (RA) is calculated by subtracting the smallest altitude from the highest one at a resolution of 90 m in each of the 1 km×1 km grid cells. The RA in the BTH region ranges from 0 to 1592 m, and was classified into six levels corresponding to the standard used for the Geomorphologic Atlas of the People's Republic of China (Cheng et al., 2011) (Table 3; Figure 4).

Most of the flat areas are found in the lower-elevation plain, the Bashang plateau, and intermontane basins of northwestern Hebei province, and these taken as a whole, cover 40.28% of the BTH region. The next two classes (< 75 m relief) are found around the margins of the Bashang plateau, in transitional areas from the lower-elevation plain to the Taihang and Yanshan mountains, and along the borders of the flat areas in the intermontane basins of northwestern Hebei province. Together, these areas total 6.75% of the BTH region. The hills that mark the borders of the lower-elevation plain, the valley zones, and front belt of the Damaqu mountains, cover 11.44% of the BTH region. The low- and middle-relief areas found in the Taihang and Yanshan mountainous regions account for about 41.26% of the BTH region. The high-relief areas mark the locations of Xiaowutai, Wuling, and Donghouding mountains.

The landform pattern of the BTH region can be described as lower-elevation plain in the southeast and mountainous areas in the western and northern parts (Figure 3). In the south, the altitude rapidly decreases from the Taihang mountains in the west to the lower-elevation plain in the east. In the north, intermontane basins alternate with high un-

Table 1 Cross-validation results of HASM-US, BR and APR

Data sets used for cross-validation	HASM-US (m)			BR (m)			APR (m)		
	MPAE	MNAE	RMSE	MPAE	MNAE	RMSE	MPAE	MNAE	RMSE
1	71	-67	21	151	-159	40	159	-156	40
2	103	-65	19	14	-211	37	15	-231	39
3	70	-61	21	21	-147	25	25	-147	25
4	28	-54	14	16	-47	16	22	-61	19
5	81	-101	29	20	-78	18	27	-93	19
6	48	-76	17	24	-79	24	29	-86	24
7	37	-101	19	30	-64	21	30	-68	22
8	41	-53	15	146	-131	32	154	-135	34
9	8	-59	16	151	-56	26	159	-56	27
10	101	-64	24	144	-95	35	152	-99	36
Mean errors	59	-70	19	72	-107	28	77	-113	28

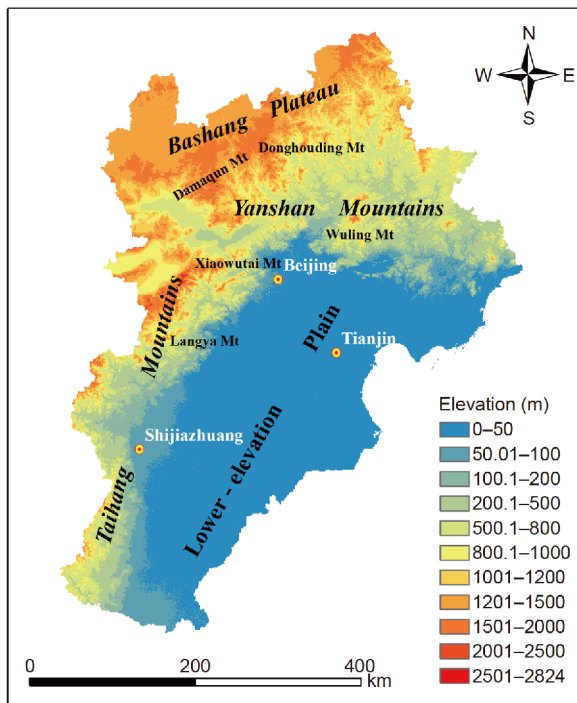


Figure 3 Elevation surface of the BTH region.

dulating mountains. In the Yanshan mountains, the altitude of the undulating terrain gradually diminishes from north to south.

3. Spatial downscaling of CMIP5 scenarios for atmospheric temperature

The spatial resolutions of many models or data are sometimes too coarse to be used for analyses at regional or local scales. To overcome this problem, many downscaling approaches have been developed to obtain information at finer resolution from the coarser resolution models and data (Yue et al., 2016a). Downscaling takes one of two forms: dynamic or statistical downscaling (Laflamme et al., 2016). Dynamic downscaling is computationally intensive and makes use of

the lateral boundary conditions combined with regional-scale forcing to produce regional climate models (RCMs) from a general circulation model (GCM). Statistical downscaling (SD) is a computationally less demanding alternative and relies on establishing statistical relationships between local climate variables and large-scale predictors. Le Roux et al. (2018) demonstrated that for an equivalent sample size it is unnecessary to dynamically downscale the simulated temperatures because statistical downscaling provides results very close to those of dynamic downscaling, while requiring much less computer resources.

We take downscaling of mean annual temperature (MAT) from CMIP5 (the fifth phase of the Coupled Model Inter-comparison Project) in the BTH region as a case study to demonstrate the essential role of both extrinsic and intrinsic properties. A MAT surface from CMIP5 at a spatial resolution of $1^\circ \times 1^\circ$ is downscaled to a corresponding surface at a spatial resolution of $1 \text{ km} \times 1 \text{ km}$, for which ground-based observations are integrated by means of HASM based downscaling method (HASM-DS) (Appendix 3).

The CMIP5 datasets of mean monthly temperature were provided by the National Climate Center of China. They include historical simulations and three Representative Concentration Pathway (RCP) scenarios: RCP2.6, RCP4.5, and RCP8.5. They were created by using the simple average of the outputs from the 21 CMIP5 models for which the spatial resolutions are unified into $1^\circ \times 1^\circ$ grids by ANUS-PLIN interpolation. Ten-day observation data of temperature were collected from 328 meteorological stations (Figure 5) scattered across and around the BTH region from 1976 to 2005 (National Meteorological Information Center of China: <http://www.nmic.gov.cn>). The upscaled elevation surface of BTH region at a spatial resolution of $1 \text{ km} \times 1 \text{ km}$ (Figure 2) was used as auxiliary data to develop the OLS regression equation.

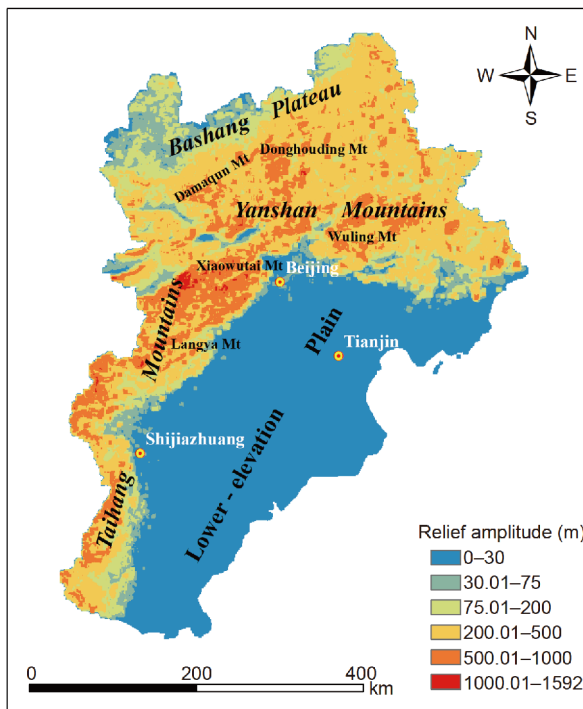
The MAT surface of CMIP5 at a spatial resolution of $1^\circ \times 1^\circ$ during the period 1976–2005 was downscaled to a corresponding surface of MAT at a spatial resolution of $1 \text{ km} \times 1 \text{ km}$ by means of HASM-DS. Eighty-five percent of the 328 meteorological stations served as optimal control constraints

Table 2 Elevation steps in the BTH region

Lower-elevation sub-region				Middle-elevation sub-region			
Step	Elevation range (m)	Area (km^2)	Proportion (%)	Step	Elevation range (m)	Area (km^2)	Proportion (%)
1	<50	80660	37.48	7	1000–1200	13490	6.27
2	50–100	14325	6.66	8	1200–1500	24972	11.60
3	100–200	9544	4.43	9	1500–2000	9764	4.54
4	200–500	21737	10.10	10	2000–2500	267	0.12
5	500–800	24804	11.53	11	>2500	17	0.01
6	800–1000	15628	7.26				
Subtotal		166698	77.46	Subtotal		48510	22.54

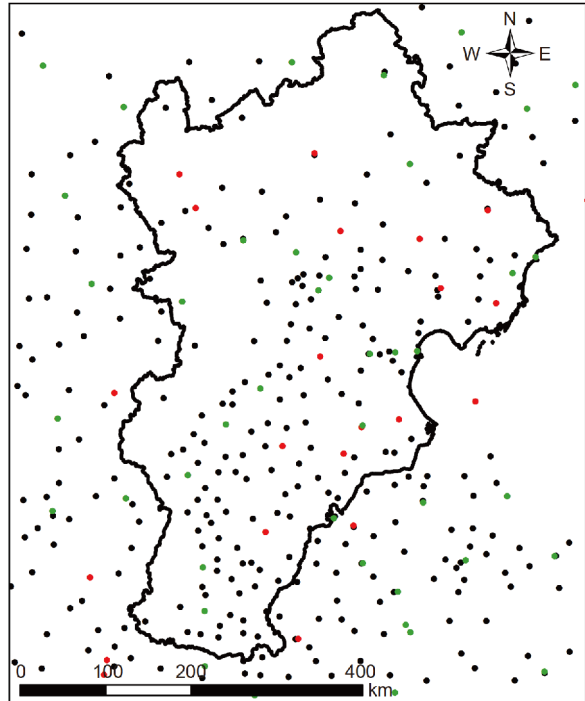
Table 3 Relief amplitude of the BTH region

Level	RA (m)	Area (km^2)	Proportion (%)
1	Flat	<30	86692
2	Platform	30–75	14526
3	Hill	75–200	24622
4	Low-relief	200–500	65218
5	Middle-relief	500–1000	23578
6	High-relief	>1000	572
	Total	215208	100

**Figure 4** Relief amplitude surface of the BTH region.

for HASM-DS and 15% of the meteorological stations were used for cross-validation. The validation results show that HASM-DS has much higher accuracy than the traditional downscaling method, ordinary linear squares (OLS-DS) (Table 4). Mean absolute errors (MAEs) of the original MAT from CMIP5, downscaled MAT by OLS-DS and downscaled MAT by HASM-DS are 1.86, 1.62 and 0.51°C, respectively; their mean relative errors are 24%, 23% and 7% and their correlation coefficients are 0.66, 0.80 and 0.96, respectively. In short, the accuracy of the original MAT was improved by 17% using HASM-DS ($p=0.05$).

The original MAT from CMIP5, downscaled MAT by OLS-DS, and downscaled MAT by HASM-DS all have an apparent regular pattern of latitude zonation during the period 1976–2005 (Figure 6). HASM-DS generated a spatial pattern with much more information using both intrinsic and extrinsic data. The results of HASM-DS show how MAT

**Figure 5** Meteorological stations scattered over and around the BTH region. All 328 stations, marked as black, green and red dots, were employed for downscaling in this section; the green and red dots are respectively used for data fusion in Section 4 and for model-data assimilation in Section 6.**Table 4** A comparison of original and downscaled MAT in the BTH region

Method	CMIP5	OLS-DS	HASM-DS
MAE (°C)	1.86	1.62	0.51
MRE (%)	24	23	7
r	0.66	0.80	0.96

declines gradually from south to north. The lowest MAT occurs in the mountainous area to the north (~2.15°C) and the highest MAT occurs on the plain in the south (14.38°C). The average MAT across the BTH region is 9.85°C.

T1, T2 and T3 are used to represent the periods 2011–2040, 2041–2070, and 2071–2100, respectively. Under the RCP2.6 scenario, MAT would increase by 0.51°C on average from T1 to T2 based on the results from HASM-DS. The increasing amplitude of MAT would step up from north to south. The largest increase, about 0.54°C, would occur around (38°N, 117°E) and the smallest increase, about 0.45°C, would occur between 42°N–43°N and 117°E–118°E. From T2 to T3, MAT would decrease by 0.09°C and the decreasing amplitude would step down from north to south. The largest drop in temperature, about 0.13°C, would occur between 42°N–43°N and 117°E–118°E and the smallest drop, about 0.07°C, would occur between 37°N–38°N.

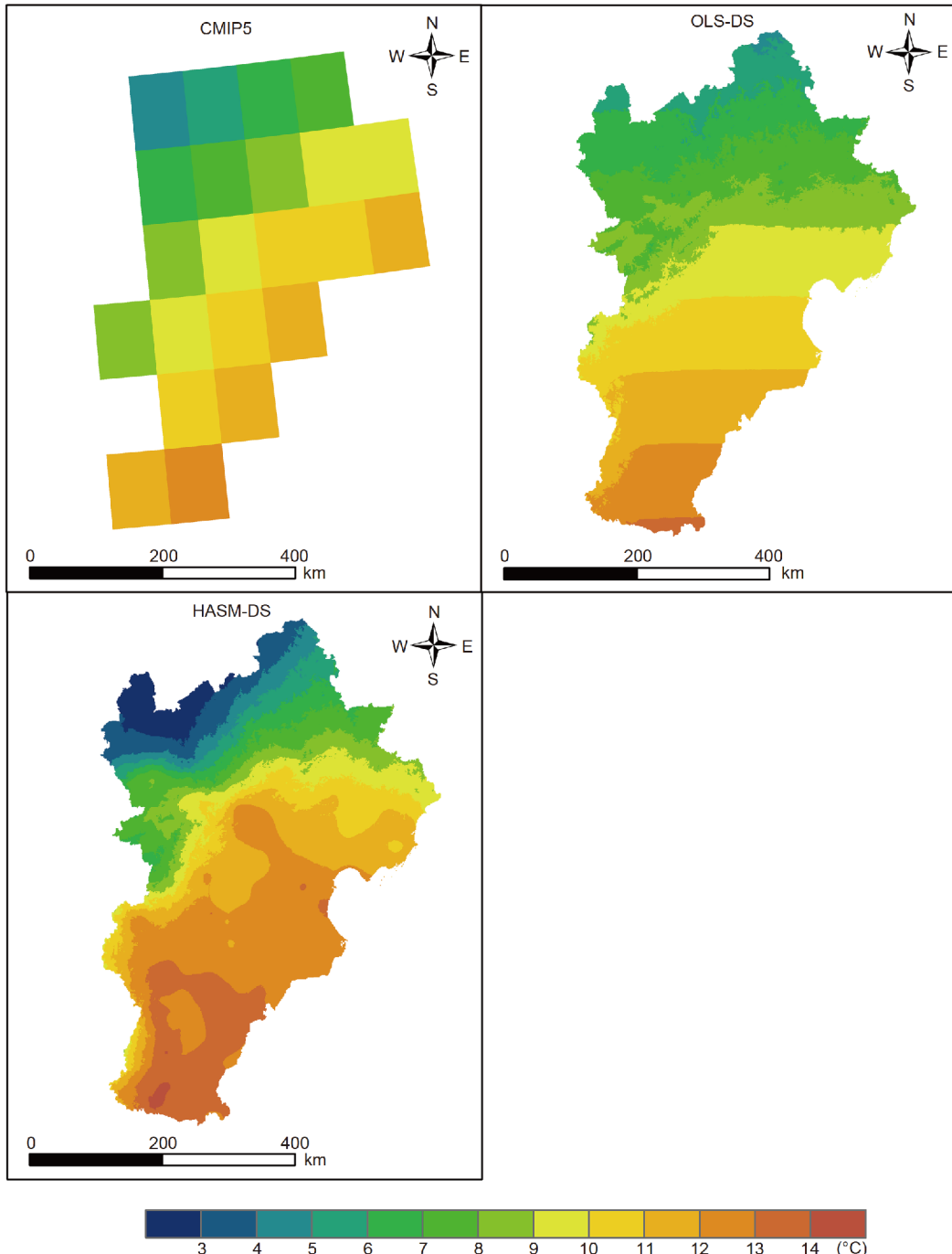


Figure 6 Spatial patterns of the original MAT from CMIP5, downscaled MAT by OLS-DS, and downscaled MAT by HASM-DS in the BTH region during the period 1976–2005.

and 117°E–118°E (Figure 7a).

Under the RCP4.5 scenario, MAT would rise 0.90°C on average from T1 to T2. The largest increase, about 0.94°C, would occur between 36°N–37°N and 113°E–114°E and the smallest increase, about 0.88°C, would occur around 39°N and 115°E–16°E. From T2 to T3, MAT would increase 49°C on average. The largest increase, about 0.51°C, would occur between 40°N–41°N and 116°E–117°E and the smallest in-

crease, about 0.43°C, would occur between 36°N–37°N and 113°E–114°E (Figure 7b).

Finally, the warming amplitude would step up from south to north during the period from T1 to T2 under RCP8.5 scenario. MAT would be 1.66°C warmer on average. The biggest warming amplitude would be 1.69°C, occurring between 42°N–43°N and 118°E and the smallest warming amplitude, about 1.59°C, would occur between 36°N–37°N

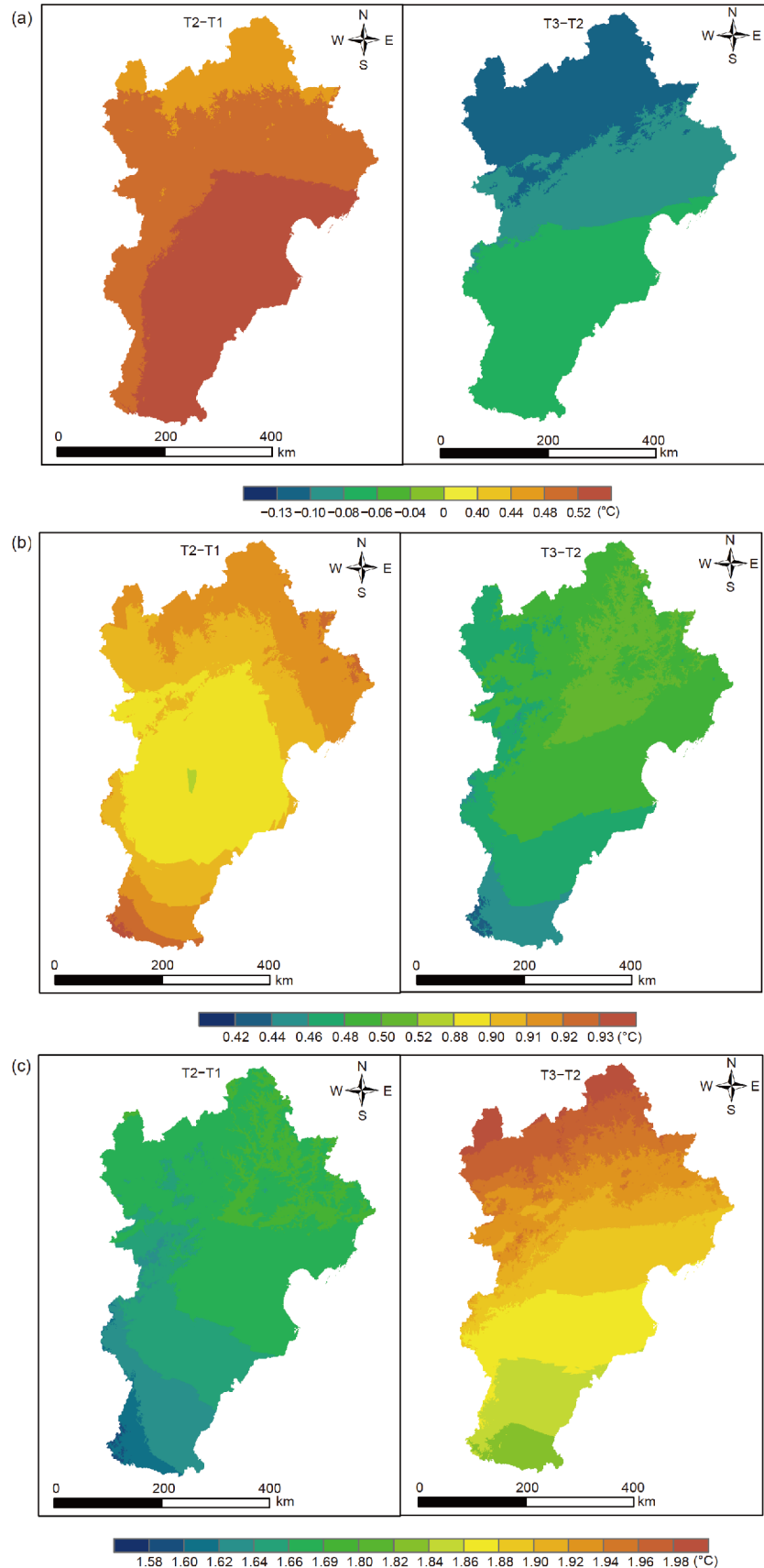


Figure 7 MAT change under scenario RCP2.6 (a), RCP4.5 (b) and RCP8.5 (c). The left map shows the subtraction of MAT in T1 from MAT in T2; the right map shows the subtraction of MAT in T2 from MAT in T3.

and 113°E–114°E. During the period from T2 to T3, MAT would increase by 1.89°C on average. The largest increase, about 1.99°C, would occur between 42°N–43°N and 117°E–118°E and the smallest increase, about 1.80°C, would occur between 36°N–37°N and 114°E–115°E (Figure 7c).

4. Data fusion of atmospheric temperature

Data fusion is the process of integrating multiple data and knowledge streams representing the same real-world object into a consistent, accurate, and useful representation. The aim of data fusion is to improve the quality of the information so that it is more accurate than one using the data sources individually (Mitchell, 2012). Since data from different sources have varying accuracy and coverage, the benefits of data fusion include improved system reliability, extended coverage and reduced uncertainty.

A subset of 49 meteorological stations, which satisfy the operational requirements of the Weather Research and Forecasting (WRF) model (Hirsch et al., 2014), were selected from the 328 stations in the BTH region and its surrounding area (Figure 5). The 49 stations provide mean daily temperature during the period 1955–2014. The residual surface, representing the difference between the WRF simulations and the observations of mean monthly temperature (MMT) at the 49 meteorological stations, was generated by the HASM-based spatial interpolation (HASM-SI). The HASM based Data Fusion (HASM-DF) of the simulated and observed MMT combines the residual surface and the MMT surface simulated by WRF (Appendix 4).

According to the leave-one-out cross-validation, the simulated temperature by WRF was cooler, compared with the observed temperatures at meteorological stations; especially, it was -1.14°C cooler in Autumn and the mean error was -0.8°C yearly (Table 5). Errors from HASM-DF data fusion ranged between -0.17 and 0.16°C during the different seasons; the mean error was only -0.02°C yearly; and the mean absolute error was reduced from 1.02°C using WRF to 0.45°C using HASM-DF. In other words, accuracy increased by 70% with the HASM-DF data fusion.

The MAT during the period 1955–2014 has a negative relation with elevation: the higher the elevation, the lower the MAT. MAT is lower than 9°C in the Yanshan and Taihang mountains, and on the Bashang plateau. The lowest MAT,

about -2.6°C , occurs at the top of Xiaowutai mountain ($39.9^{\circ}\text{N}, 115.0^{\circ}\text{E}$), where the altitude exceeds 2500 m, and the snow cover persists for about nine months. MAT ranged from 9 to 14°C in the lower-elevation plain. MAT was higher than 13°C south of 38°N and in the urban areas of Beijing and Tianjin because of the urban heat island effect (Figure 8).

The decadal periods 1955–1964, 1965–1974, 1975–1984, 1985–1994, 1995–2004, and 2005–2014 are respectively referred to as p1, p2, p3, p4, p5, and p6 below. From p1 to p2, MAT decreased in the center of the BTH region, but MAT slightly increased in the south and north. MAT increased by 0.2 – 0.6°C in most of the BTH region from p2 to p3, and by 0 – 0.4°C from p3 to p4. The warming amplitude stepped up gradually from east to west during the period from p4 to p5, exceeding 0.8°C in the western part of the BTH region. From p5 to p6, the warming amplitude ranged from -0.2 to 0.2°C and the extent of the warmer area was similar to the cooler area (Figure 9).

The 12 months of the year were next divided into 4 seasons: Spring (March–May), Summer (June–August), Autumn (September–November), and Winter (December–February). The Mann-Kendall trend test statistic (Mann, 1945; Hamed, 2009) showed that mean seasonal temperature (MST) had increasing trends in all seasons ($p=0.01$) (Table 6), but their warming rates varied considerably.

In spring, the warming rate was $0.040^{\circ}\text{C yr}^{-1}$; the lowest MST was 8.3°C in 1956 and the highest MST of 13.0°C occurred in 2014. MST increased from north to south in the BTH region from p1 to p2. The change in MST ranged from 0 to -0.4°C in the north and by 0.4°C or more south of 39°N . From p2 to p3, most of the BTH region became warmer with the largest increases of more than 0.6°C occurring in the northeast. From p3 to p4, warming dominated north and cooling dominated south of 39°N . From p4 to p5, the BTH region had the fastest warming rate, compared with the other decadal periods. The warming rate gradually increased from east to west and exceeded 1°C in the western BTH region. From p5 to p6, the areas north of 40°N were dominated by cooling and those south of 40°N were dominated by warming; the largest cooling rate, about -0.4°C , occurred in the north and the largest warming rate, about 0.4°C , occurred in the south (Figure 10).

In summer, the warming rate was $0.019^{\circ}\text{C yr}^{-1}$, which was the slowest rate among the four seasons; the lowest MST of

Table 5 A statistical comparison of WRF and HASM-DF errors

	Method	Spring (°C)	Summer (°C)	Autumn (°C)	Winter (°C)	On average (°C)
Mean error	WRF	-0.86	-0.22	-1.14	-0.98	-0.80
	HASM	0.16	0.05	-0.12	-0.17	-0.02
Mean absolute error	WRF	1.48	0.70	1.15	1.16	1.02
	HASM	0.63	0.42	0.44	0.62	0.45

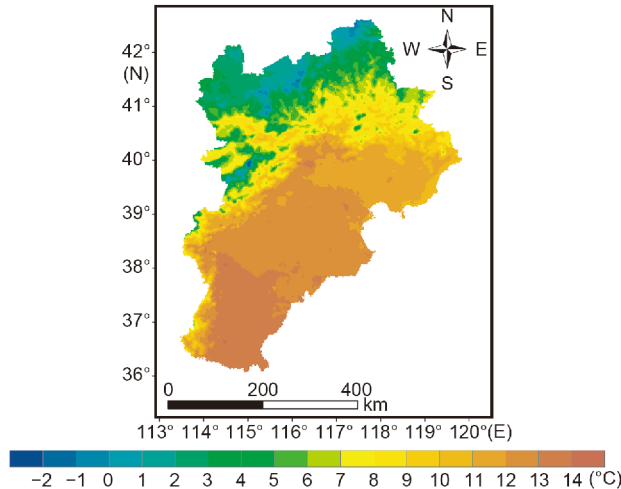


Figure 8 Spatial pattern of MAT in the BTH region during the period 1955–2014.

20.9°C and highest MST of 24.2°C occurred in 1976 and 2000, respectively. The MST declined from p1 to p2 with the exception of the northwestern Bashang plateau and a small

area in the south. The cooling rate exceeded -0.4°C in the center of the BTH region. From p2 to p3, the northeast experienced a warming trend but the south and northwest areas experienced a cooling trend. The largest warming and cooling rates were 0.4 and -0.4°C , respectively. From p3 to p4, the BTH region experienced a warming trend with an amplitude of about 0.2°C . From p4 to p5, the whole BTH region experienced a warming trend and the amplitude exceeded 0.6°C in some areas such as Beijing. From p5 to p6, warming dominated the BTH region with warming rates ranging from 0.2 to 0.4°C (Figure 11).

In autumn, the warming rate was $0.025^{\circ}\text{C yr}^{-1}$, slightly higher than in summer. The lowest and highest MSTs were 8.1 and 11.7°C and occurred in 1981 and 2006, respectively. The MST ranged from -0.2°C to 0.2°C and the cooling occurred between 38°N – 41°N and 116°E – 118.5°E from p1 to p2. From p2 to p3, the entire BTH region experienced a warming trend ranging from 0.2 to 0.6°C and the area between 37.5°N – 39.5°N and 115°E – 118°E experienced a higher warming rate, ranging from 0.4 to 0.6°C . From p3 to p4, warming weakened and some areas across the BTH re-

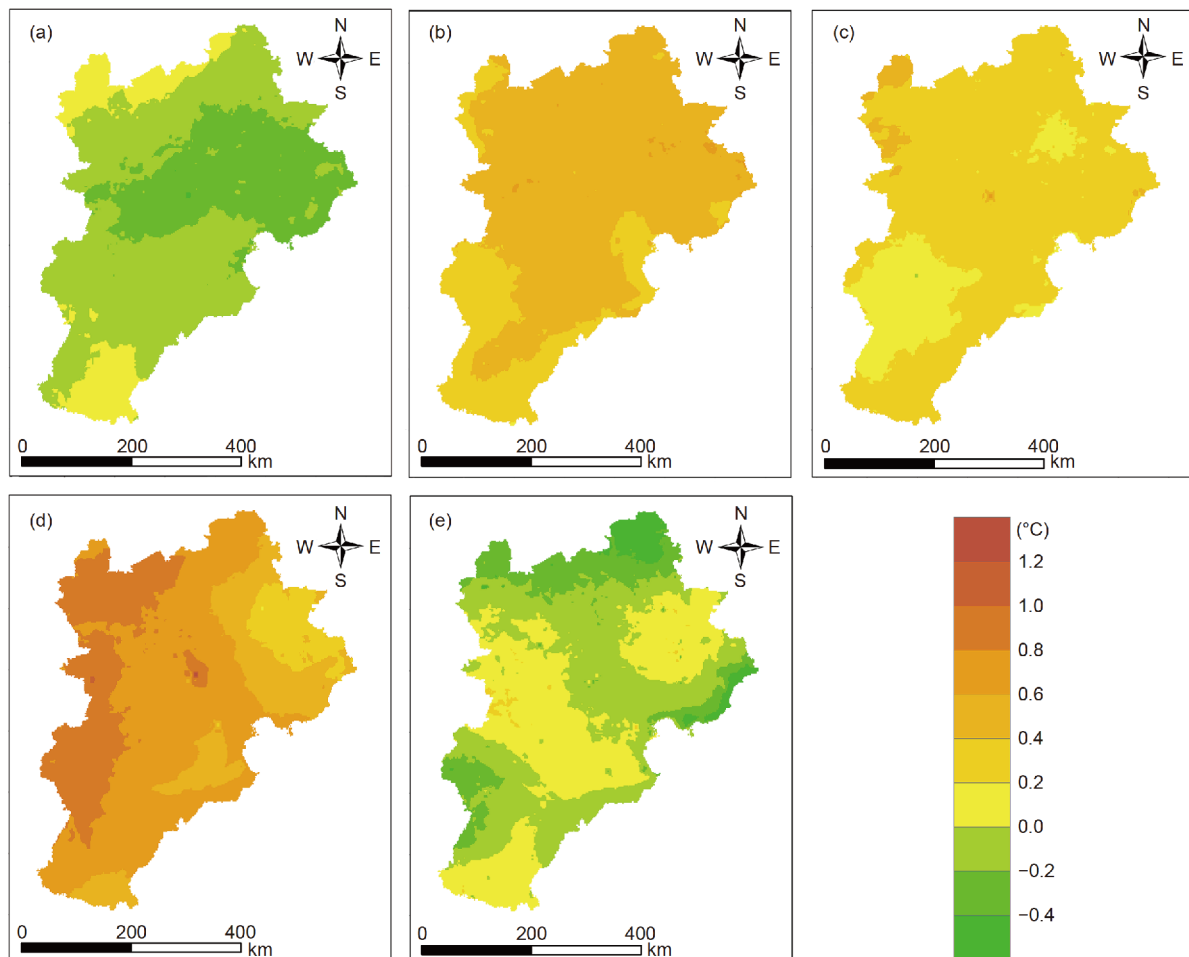


Figure 9 MAT change by decade. (a) Subtraction of MAT in p1 from MAT in p2; (b) subtraction of MAT in p2 from MAT in p3; (c) subtraction of MAT in p3 from MAT in p4; (d) subtraction of MAT in p4 from MAT in p5; and (e) subtraction of MAT in p5 from MAT in p6.

Table 6 The Mann-Kendall trend test statistic of mean annual temperature and mean seasonal temperature during the period from 1955 to 2014 in the BTH region^{a)}

	Trend	Warming rate (°C yr ⁻¹)	Confidence level	R
Spring	↑	0.040	99%	0.61
Summer	↑	0.019	99%	0.46
Autumn	↑	0.025	99%	0.53
Winter	↑	0.039	99%	0.51
Annual	↑	0.030	99%	0.71

a) “↑” denotes an increasing trend

gion became cooler. From p4 to p5, the majority of the BTH region experienced warming with rates exceeding 0.4°C to the west of 115°E and in Beijing and Tianjing. However, the northeastern Yanshan mountains experienced a cooling trend from p4 to p5. From p5 to p6, the BTH region grew warmer with warming rates to the south of 37°N and north of 38°N exceeding 0.4°C (Figure 12).

In winter, which experienced the highest warming rate among the four seasons, the warming rate was 0.039°C yr⁻¹;

the lowest and highest MSTs were -8.5 and -2.6°C in 1969 and 2007. Cooling rates exceeding -0.4°C prevailed across most of the BTH region from p1 to p2 and from p5 to p6. However, the entire BTH region grew warmer during the three decades from p2 to p5. Warming rates exceeded 1.2°C in the western and southern parts of the BTH region from p2 to p3 and in the western BTH region and Beijing from p4 to p5. From p3 to p4, the warming amplitude was slightly smaller, but most areas still experienced warming rates ranging from 0.6 to 0.8°C (Figure 13).

In short, the warming rates were faster in spring and winter. All of the highest MST have occurred since 2000. The annual warming rate averaged 0.030°C yr⁻¹ during the period 1955–2014 in the BTH region, which was much higher than the 0.012°C yr⁻¹ average global warming rate.

5. Spatial interpolation of mean annual precipitation

Spatial interpolation is used to predict the values of a primary

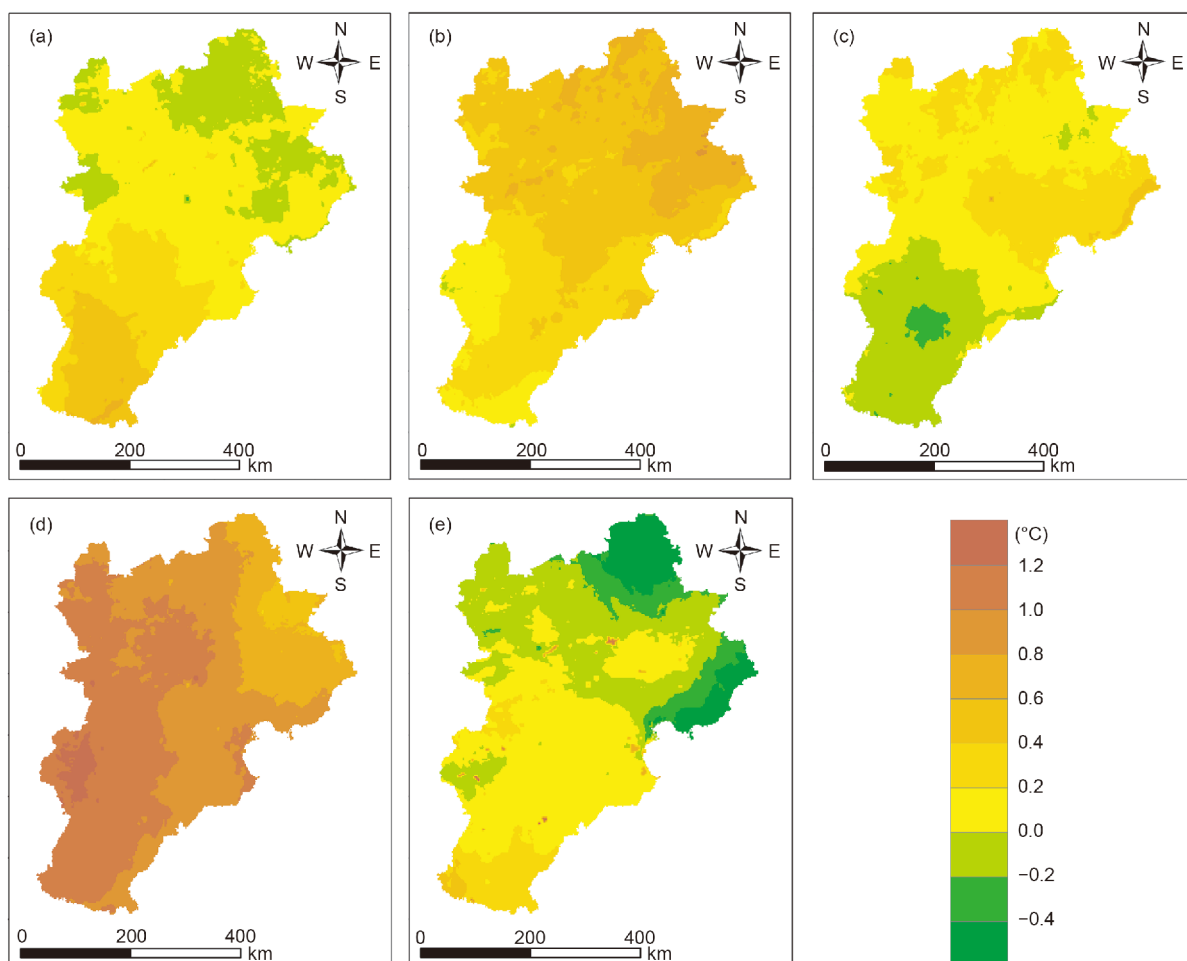


Figure 10 MST change in spring. (a) Subtraction of MST in p1 from MST in p2; (b) subtraction of MST in p2 from MST in p3; (c) subtraction of MST in p3 from MST in p4; (d) subtraction of MST in p4 from MST in p5; and (e) subtraction of MST in p5 from MST in p6.

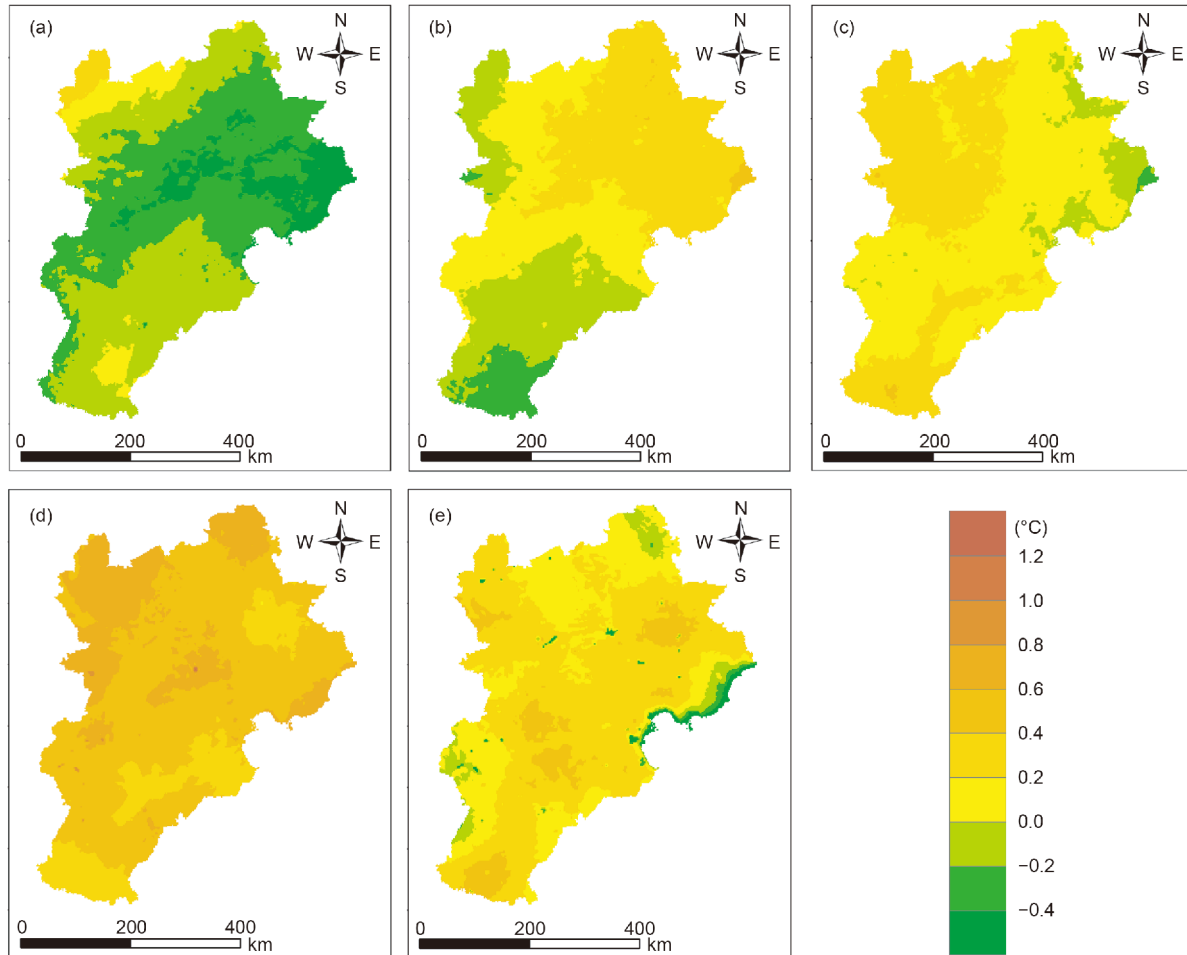


Figure 11 MST change in summer. (a) Subtraction of MST in p1 from MST in p2; (b) subtraction of MST in p2 from MST in p3; (c) subtraction of MST in p3 from MST in p4; (d) subtraction of MST in p4 from MST in p5; and (e) subtraction of MST in p5 from MST in p6.

variable at points within the same region of sampled locations in terms of spatial data in the form of discrete points or some form of a surface with data voids (Li and Heap, 2014). Spatial interpolation provides an effective means to construct a continuous surface from discrete data or a surface with missing data (Wang and Wang, 2012). Almost all spatial interpolation methods rely on local weighting, except for HASM-SI that provides a finite difference method (Appendix 5).

A statistical analysis demonstrated that mean annual precipitation (MAP) is non-stationary in the BTH region. HASM-SI expresses extrinsic information of MAP by geographically weighted regression (GWR) using data from the selected meteorological stations for spatial interpolation, for which the upscaled elevation surface of the BTH region (Figure 3) was employed as auxiliary data. Intrinsic information is the interpolated bias correction at every lattice cell of the GWR surface of MAP. Among the 328 meteorological stations, 85% were randomly selected for spatial interpolation and 15% were used for cross-validation. The

validation results show that HASM-SI has higher accuracy than the classic methods, such as inverse distance weighting (IDW), ordinary Kriging (OK) and splines (Table 7; Figure 14). The mean relative errors (MREs) of IDW, OK, spline and HASM-SI are 4.2, 3.7, 4.0 and 3.5% and their correlation coefficients are 0.928, 0.941, 0.913 and 0.943, respectively ($p=0.05$).

In the northern BTH region, precipitation is affected by the Taihang and Yanshan mountains. The areas to the east of the Taihang mountains and south of the Yanshan mountains have much higher precipitation. The largest MAP is 711 mm in terms of HASM-SI, occurring between 40°N – 41°N and 118°E – 119°E . In the Bashang plateau and northern Taihang mountains, MAP ranges from 186 to 450 mm with the lowest MAP occurring around $(40^{\circ}\text{N}, 115^{\circ}\text{E})$. To the south of 39°N , MAP varies from ~450 to 550 mm, but there is less precipitation in the central area and more precipitation in the western and eastern areas.

MAP surfaces of the BTH region for the periods 1976–1985, 1986–1995, 1996–2005, 2006–2015, which are re-

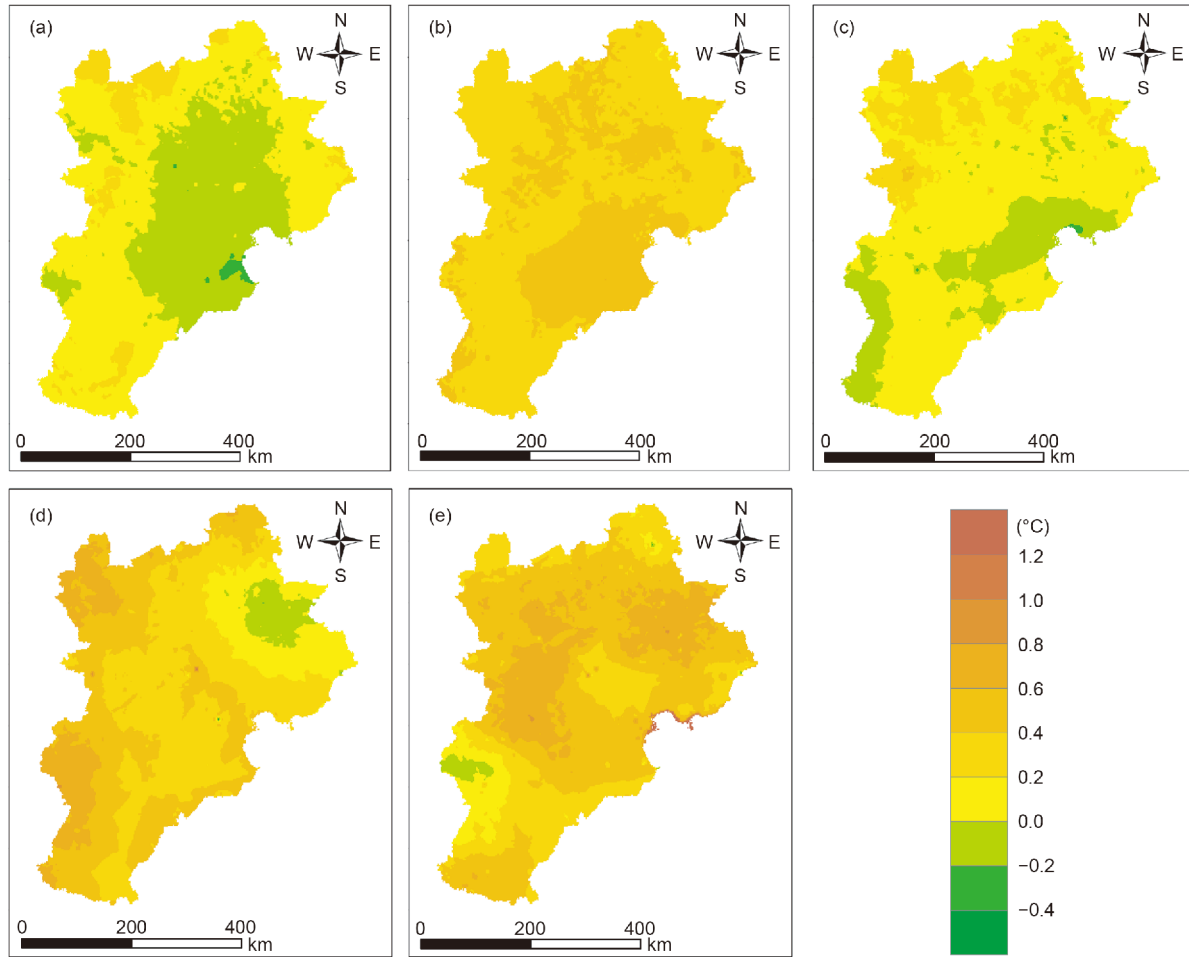


Figure 12 MST change in autumn. (a) Subtraction of MST in p1 from MST in p2; (b) subtraction of MST in p2 from MST in p3; (c) subtraction of MST in p3 from MST in p4; (d) subtraction of MST in p4 from MST in p5; and (e) subtraction of MST in p5 from MST in p6.

spectively represented by t1, t2, t3 and t4, were created by HASM-SI using precipitation data from the 328 meteorological stations (Figure 5) and taking the upscaled elevation surface as auxiliary data (Figure 3). The results indicated that the BTH region became wetter and MAP increased by 12 mm on average during the period from t1 to t2. The highest increasing amplitude was 189 mm, which occurred near (41°N, 118°E). From t2 to t3, precipitation decreased, especially on the lower-elevation plain. MAP decreased by 58 mm over the BTH region on average. The largest drop (167 mm) occurred between 38°N–39°N and 116°E. However, MAP showed an increasing trend on the Bashang plateau and in the south. The largest increase (80 mm) occurred between 40°N–41°N and 117°E–118°E. From t3 to t4, precipitation increased over the majority of the BTH region and especially in the lower-elevation plain, but decreased in the Yanshan and Taihang mountains. MAP increased by 30 mm over the BTH region on average. The largest increase (159 mm) occurred between 38°N–39°N and 116°E–117°E. The largest drop of MAP (193 mm) occurred 40°N–41°N

and 119°E–120°E.

During the period from 1976 to 2015, MAP declined at a rate of $-5.54 \text{ mm} (10 \text{ yr})^{-1}$ on average across the BTH region. The largest decreasing amplitude was $-40.78 \text{ mm} (10 \text{ yr})^{-1}$, which occurred between 40°N–41°N and 117°E–118°E. However, MAP displayed increasing rates in many areas scattered across the BTH region, with the largest increase (27.70 mm) occurring between 37°N–38°N and 117°E–118°E (Figure 15).

6. Model-data assimilation of carbon stocks

Model-data assimilation (MDA) includes model inversion and data assimilation. Data assimilation seeks to improve the performance of a model by either optimizing parameters or initial state variables according to a given data set (Peng et al., 2011). Model inversion seeks to estimate parameters that are related to the measured quantity, by using observed properties to constrain physical or biological processes.

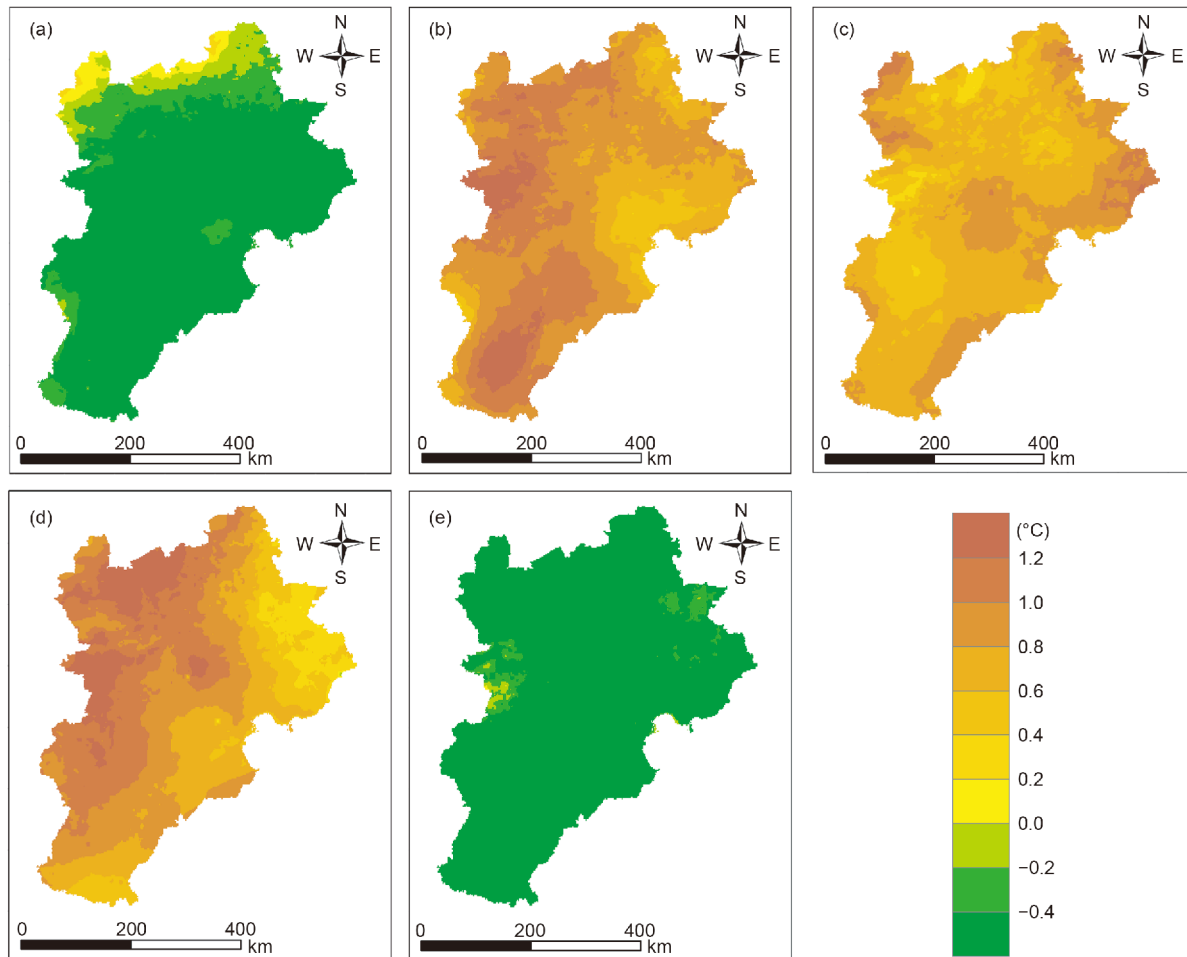


Figure 13 MST change in winter. (a) Subtraction of MST in p1 from MST in p2; (b) subtraction of MST in p2 from MST in p3; (c) subtraction of MST in p3 from MST in p4; (d) subtraction of MST in p4 from MST in p5; and (e) subtraction of MST in p5 from MST in p6.

Table 7 Comparison of errors from different interpolation methods

Method	IDW	OK	Spline	HASM-SI
MAE (mm)	22	19	20	18
MRE (%)	4.2	3.7	4.0	3.5
R	0.928	0.941	0.913	0.943

System models and observations provide abundant streams of information, but none of them provides the complete picture (Ponsar et al., 2016). A system model, if it is to be as accurate as possible, must supplement information from the currently available ground observations (Brill et al., 1991). The aim of MDA is to use measured observations in combination with a system model in order to derive accurate estimates of the current and future states of the system, together with estimates of the uncertainty in the estimates of current or future states (Nichols, 2010). The MDA power is not only based on its ability to produce forecasts of the dynamic model, but also to make inferences about quantities that are otherwise hidden from observations (Li et al., 2014).

In this case, a model-data assimilation algorithm is developed on the basis of HASM under the framework of the Lund-Potsdam-Jena General Ecosystem Simulator (LPJ-GUESS), an integrated model of the Lund-Potsdam-Jena dynamic global vegetation model (LPJ-DGVM) and the General Ecosystem Simulator (GUESS) (Smith et al., 2001, 2014; Bagnara et al., 2019). The HASM based model-data assimilation (HASM-MD) (Appendix 6) was used to support surface modelling of carbon stocks with a continuous time series by introducing changing curves of state variables with time into the HASM algorithm at three spatial dimensions.

The plant functional types (PFTs) in LPJ-GUESS are modified by taking the Vegetation Map of the People's Republic of China as a reference (Editorial Committee of Vegetation Map of China, 2007). The modified PFTs in the BTH region include cold-temperate and temperate deciduous coniferous forests, cold-temperate and temperate mountainous needle-leaf forest, temperate needle-leaf forest, temperate broad-leaf deciduous forest and temperate grassland (C3). The climatic parameters were adjusted to match the

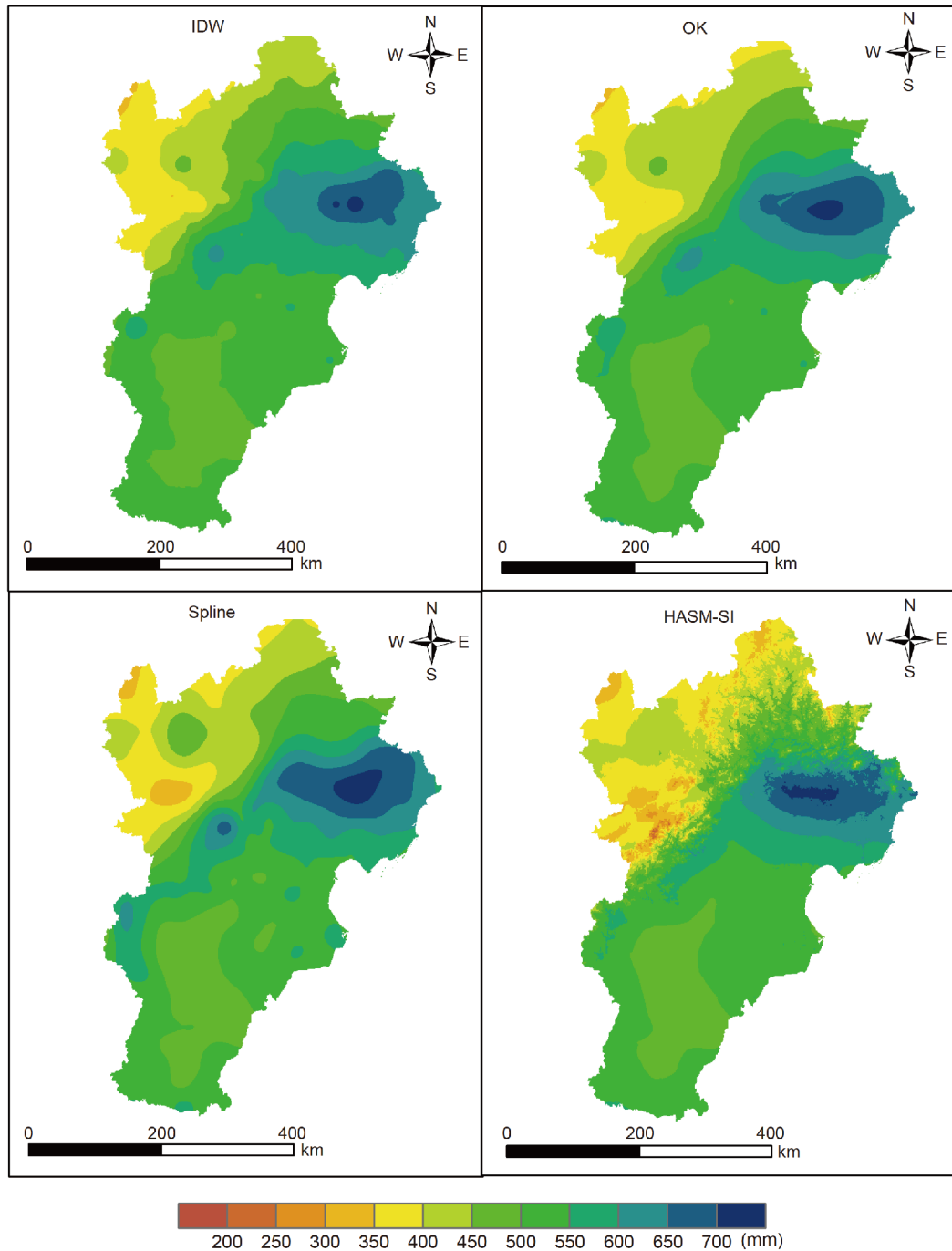


Figure 14 Comparative maps of mean annual precipitation from different methods for spatial interpolation.

modified PFTs in the BTH region, such as MMT in the coldest and warmest months as well as accumulated temperature for survival and establishment of the plant functional types (Table 8).

Climatic data for driving the LPJ-GUESS model include mean monthly temperature, precipitation, sunshine percentage and number of rainy days, and the mean annual atmospheric CO₂ concentration. The point data came from 65 meteorological stations, selected from the 328 meteor-

ological stations scattered across and around the BTH region. The surface data were produced by using HASM with the point data.

Forest cover maps in 2003, 2008 and 2013 were developed on the basis of the national forestry inventory during the periods 1999–2003, 2004–2008, and 2009–2013 (Figure 16). The carbon stocks data for validation was collected from 121 sample spots during the period 2013–2017. The measured parameters included diameter of a cross-section of a tree

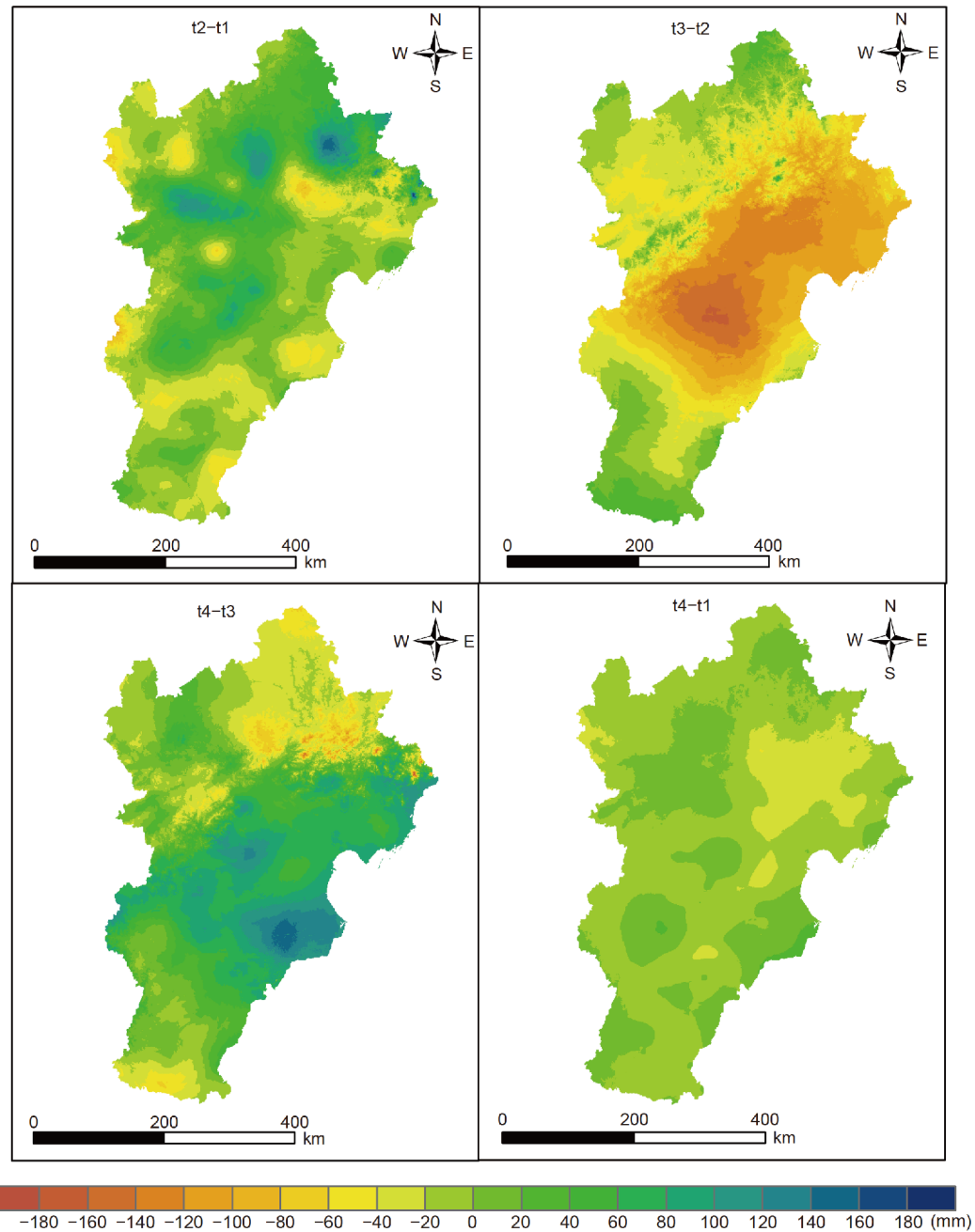


Figure 15 Change trend of precipitation in the BTH region. (a) Left upper map shows the subtraction of MAP in t1 from MAP in t2; (b) right upper map shows the subtraction of MAP in t2 from MAP in t3; (c) left lower map shows the subtraction of MAP in t3 from MAP in t4; and (d) right lower map shows the subtraction of MAP in t1 from MAP in t4.

Table 8 Climatic parameters distinguishing the five plant functional types (PFTs)^{a)}

PFT	$T_{c,\min}$ (°C)	$T_{c,\max}$ (°C)	$T_{w,\max}$ (°C)	$T_{w-c,\min}$ (°C)	GDD _{min} (°C)
Cold-temperate and temperate deciduous coniferous forests	–	-13	23.5	35	350
Cold-temperate and temperate mountainous needle-leaf forest	-32.5	-13	23.5	–	600
Temperate needle-leaf forest	-13	3	–	–	900
Temperate broad-leaf deciduous forest	-32.5	3	–	–	1200
Temperate grassland (C3)	–	14	–	–	0

a) $T_{c,\min}$ and $T_{c,\max}$ are the lower and upper limits of mean monthly temperature (MMT) in the coldest month, respectively; $T_{w,\max}$ is the upper limit of MMT in the warmest month; $T_{w-c,\min}$ is the lower limit of difference between MMT in the warmest and the coldest months; and GDD_{min} is the lower limit of accumulated temperature for survival and establishment

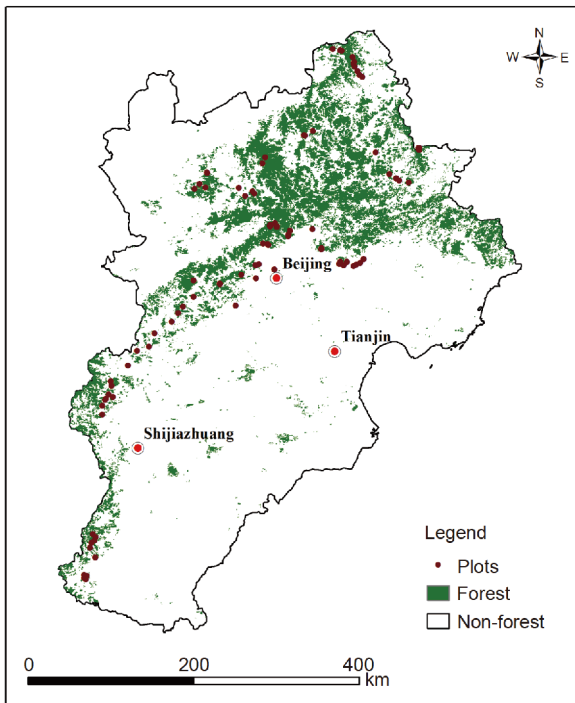


Figure 16 Forest cover and sample plots in the BTH region.

trunk at 1.3 m above the ground, tree species, tree height and the geographic coordinates of the tree. The biomass of the tree was calculated using the single-tree biomass equation. The carbon stocks of the tree were the product of the carbon content and biomass (Li and Lei, 2010). The validation results indicated that the mean absolute and relative errors for the model were 2.084 kg m^{-2} and 68%, and HASM-MD provided estimates of were 0.848 kg m^{-2} and 28%, respectively. In other words, model-data assimilation improved the

accuracy of LPJ-GUESS by 40% and using HASM-MD provided estimates of 37.14 km^2 , 3.074 kg m^{-2} and 114.17 Tg, for the forest area, carbon density and carbon stocks in the BTH region, respectively in 2013.

The Mann-Kendall approach to trend analysis (Mann, 1945; Kendall, 1948) was employed to characterize the change trend of forest area (FA). The results showed that FA had an obvious increasing trend during the period from 2001 to 2015. The mean increment was $1.18 \times 10^5 \text{ km}^2 \text{ yr}^{-1}$ ($\beta=1.325$, $p=0.001$). FA increased by 75% from 2001 to 2015. The largest increment occurred in 2008, following an average increment rate of $0.34 \times 10^5 \text{ hm}^2 \text{ yr}^{-1}$ ($\beta=0.311$, $p=0.005$) prior to 2008 and a net decline ($\beta=-0.193$, $p=0.1$) after 2008.

Forest carbon stocks (CS), caused by afforestation, had a strong upward trend ($\beta=4.325$, $p=0.01$) during the period 2001–2015. The CS increased by 90% from 2001 to 2015, growing by 20 Tg yr^{-1} on average. The forest carbon density (CD) also displayed an upward trend ($\beta=0.012$, $p=0.01$). The CD increased by 9% from 2001 to 2015, growing at the rate of $0.017 \text{ kg m}^{-2} \text{ yr}^{-1}$ on average. However, the net increment of CS was not as strong ($\beta=0.003$, $p=0.1$) because the net increment (0.641 Tg yr^{-1}) for this metric displayed an upward trend prior to 2008 ($\beta=0.603$, $p=0.05$) and an obvious downward trend ($\beta=-0.403$, 0.1) after 2008.

The CS was divided between the original forest (OCS), which existed before 2001, and afforestation (ACS), the forest planted since 2001, in order to identify relationship between CS and forest cover change during the period 2001–2015 (Figure 17). The carbon density of the original forest had an obvious upward trend ($\beta=0.255$, $p=0.01$) such that the carbon density increased by 3.518 kg m^{-2} , but the OCS decreased by 10.035 Tg because the original forest cover de-

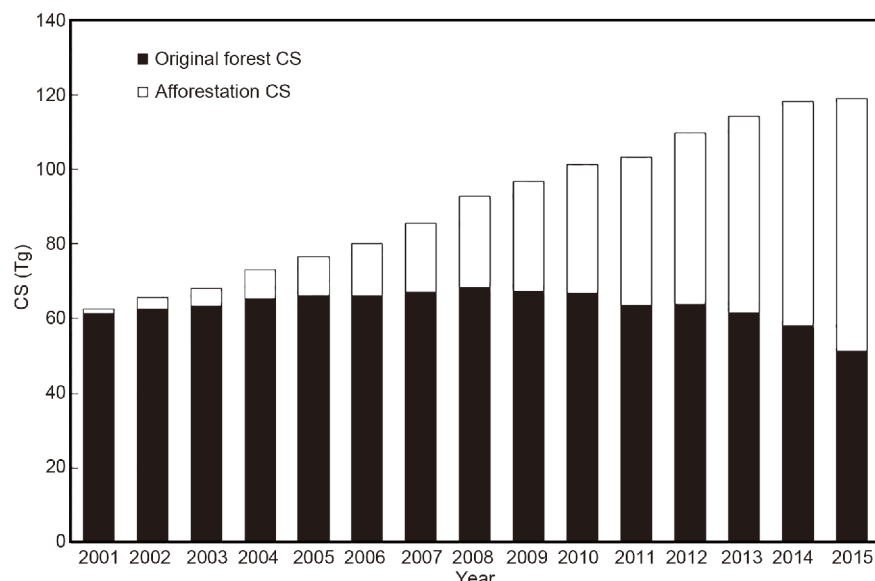


Figure 17 Contributions of original forest and afforestation to total carbon stocks by year.

clined during the period 2001–2015. The ACS had a continuous upward trend, and increased by 67.687 Tg during the same period ($\beta=4.765$, $p=0.01$).

The net effect of forest cover change to carbon stocks changed from a negative to a positive contribution in 2006 and during the period 2011–2015, the CS increment of afforestation was 4.512 Tg yr^{-1} and the CS loss due to deforestation and tree mortality was 4.147 Tg yr^{-1} . The contribution of forest cover change to CS, jointly caused by afforestation and deforestation, changed from -1.996 to 3.656 Tg yr^{-1} from 2001 to 2015.

In short, the forest area increased at a rate of 1180 $\text{km}^2 \text{yr}^{-1}$ and the net increment was 16550 km^2 , in which forest area increased by 29350 km^2 because of afforestation and decreased by 12800 km^2 because of deforestation during the period 2001–2015. The CS had an increment rate of 4.020 Tg yr^{-1} . The total increase was 56.282 Tg over the 15 years, of which the original forest and afforestation contributed 48.807 and 66.317 Tg, respectively and deforestation removed 58.841 Tg. Carbon density increased from 2.839 kg C m^{-2} in 2001 to 3.079 kg C m^{-2} in 2015.

7. Discussion and conclusions

The aforementioned examples show how the HASM-based methods have greatly improved the modeling of the Earth's surface systems in the BTH region by integrating intrinsic and extrinsic information. The methods, which included spatial upscaling, spatial downscaling, spatial interpolation, data fusion and model-data assimilation, were used to simulate an elevation surface, the change trend and scenarios of atmospheric temperature, precipitation change, and the increment of carbon stocks. The spatiotemporal characteristics of these surfaces were portrayed in the kinds of detail needed to understand and anticipate key processes and trends moving forward.

This said, there are five outstanding mathematical and three technical questions that still need to be answered to further improve the HASM system for earth surface modeling.

The five mathematical questions are: (1) What is the physical meaning of the Weingarten and Codazzi equation sets? (2) Can the HASM optimal control constraints can be substituted and used in place of the Weingarten equation or not? (3) What is the mathematical explanation for how the finite difference discretization of HASM extended the capacity of the fundamental theorem of surfaces to provide local to global solutions? (4) How does adopting or discarding the cross-term equation in the HASM equation set affect simulation error of HASM? (5) How do the various parameters included in HASM affect the solution accuracy and computing speed?

The three technical questions are: (1) How to capture and

model the features, such as cliffs and fracture zones, which change quickly and the organic transitions between these and smooth areas? (2) How to incorporate advanced computational methods in HASM to support work with large datasets? (3) How to find one or more solutions for modeling in four dimensions and supporting dynamic simulations in three dimensions?

In closing, it is also the case that no single model can capture all of the dynamics of the Earth's surface at a high level of detail. The coupling of models may provide an alternative solution because the outputs of one model can serve as input to another model by loose or tight coupling, and thereby allow feedback (IPBES, 2016). The choice of tight versus the loose coupling depends on the specific requirements of the system under consideration. A loosely coupled model approach allows for the identification of the role of system interactions, whereas a tight coupling approach will be required when feedback between the system components is important to the outcomes. Further clarification and assessment of the advantages and disadvantages of the various options for coupling HASM and related models is another focus of our future work.

Acknowledgements All data, corresponding to Figures 3–17, can be found from appended datasets at <https://link.springer.com/journal/11430>. This work was supported by the National Natural Science Foundation of China (Grant Nos. 41930647, 41590844, 41421001 & 41971358), the Strategic Priority Research Program (A) of the Chinese Academy of Sciences (Grant No. XDA20030203), the Innovation Project of LREIS (Grant No. O88RA600YA) and the Biodiversity Investigation, Observation and Assessment Program (2019–2023) of the Ministry of Ecology and Environment of China.

References

- Akima H. 1978a. A method of bivariate interpolation and smooth surface fitting for irregularly distributed data points. *ACM Trans Math Softw*, 4: 148–159
- Akima H. 1978b. Algorithm 526: Bivariate interpolation and smooth surface fitting for irregularly distributed data points. *ACM Trans Math Softw*, 4: 160–164
- Bagnara M, Silveyra Gonzalez R, Reifenberg S, Steinkamp J, Hickler T, Werner C, Dornmann C F, Hartig F. 2019. An R package facilitating sensitivity analysis, calibration and forward simulations with the LPJ-GUESS dynamic vegetation model. *Environ Model Softw*, 111: 55–60
- Bengtsson B E, Nordbeck S. 1964. Construction of isarithms and isarithmic maps by computers. *BIT*, 4: 87–105
- Birkhoff G, Garabedian H L. 1960. Smooth surface interpolation. *J Math Phys*, 39: 258–268
- Brill K F, Uccellini L W, Manobianco J, Kocin P J, Homan J H. 1991. The use of successive dynamic initialization by nudging to simulate cyclogenesis during GALE IOP 1. *Meteorol Atmos Phys*, 45: 15–40
- Chen C F, Yue T X. 2010. A method of DEM construction and related error analysis. *Comput Geosci*, 36: 717–725
- Chen C F, Yue T X, Dai H L, Tian M Y. 2013a. The smoothness of HASM. *Int J Geogr Inf Sci*, 27: 1651–1667
- Chen C F, Li Y Y, Yue T X. 2013b. Surface modeling of DEMs based on a sequential adjustment method. *Int J Geogr Inf Sci*, 27: 1272–1291
- Cheng W M, Zhou C H, Chai H X, Zhao S M, Liu H J, Zhou Z P. 2011. Research and compilation of the geomorphologic atlas of the People's

- Republic of China (1:1000000). *J Geogr Sci*, 21: 89–100
- Crow W T, Berg A A, Cosh M H, Loew A, Mohanty B P, Panciera R, de Rosnay P, Ryu D, Walker J P. 2012. Upscaling sparse ground-based soil moisture observations for the validation of coarse-resolution satellite soil moisture products. *Rev Geophys*, 50: RG2002
- De Boor C. 1962. Bicubic spline interpolation. *J Math Phys*, 41: 212–218
- Djaferis T E, Schick I C. 2000. System theory: Modeling, analysis, and control. Boston: Kluwer
- Editorial Committee of Vegetation Map of China. 2007. Vegetation map of the People's Republic of China. Beijing: Geological Publishing House
- Evans I S. 1980. An integrated system of terrain analysis and slope mapping. *Z Geomorphol Suppl Bd*, 36: 274–295
- Foley T A, Nielson G M. 1980. Multivariate interpolation to scattered data using delta iteration. In: Cheney E W, ed. *Approximation Theory III*. New York: Academic Press
- Franke R. 1982. Scattered data interpolation: Tests of some methods. *Math Comput*, 38: 181
- Fry J, Guber A K, Ladoni M, Munoz J D, Kravchenko A N. 2017. The effect of up-scaling soil properties and model parameters on predictive accuracy of DSSAT crop simulation model under variable weather conditions. *Geoderma*, 287: 105–115
- Hamed K H. 2009. Exact distribution of the Mann-Kendall trend test statistic for persistent data. *J Hydrol*, 365: 86–94
- Harder R L, Desmarais R N. 1972. Interpolation using surface Splines. *J Aircraft*, 9: 189–191
- Hirsch A L, Pitman A J, Seneviratne S I, Evans J P, Haverd V. 2014. Summertime maximum and minimum temperature coupling asymmetry over Australia determined using WRF. *Geophys Res Lett*, 41: 1546–1552
- Hull D J. 2003. *Optimal Control Theory for Applications*. New York: Springer
- IPBES (The Intergovernmental Science-Policy Platform on Biodiversity and Ecosystem Services). 2016. *The Methodological Assessment Report on Scenarios and Models of Biodiversity and Ecosystem Services*. Secretariat of the Intergovernmental Science-Policy Platform on Biodiversity Ecosystem Services, Bonn, Germany
- IPBES (The Intergovernmental Science-Policy Platform on Biodiversity and Ecosystem Services). 2019. *Global Assessment on Biodiversity and Ecosystem Services*. Secretariat of the Intergovernmental Science-Policy Platform on Biodiversity Ecosystem Services, Bonn, Germany
- Isaaks E H, Srivastava R M. 1989. *Applied Geostatistics*. New York: Oxford University Press
- Kendall M G. 1948. Rank Correlation Methods. London: Griffin
- Kerimov I A. 2009. F-approximation of the Earth's surface topography. *Izv Phys Solid Earth*, 45: 719–729
- Krige D G. 1951. A statistical approach to some basic mine valuation problems on the Witwatersrand. *J Chem Metall Min Soc South Africa*, 52: 119–139
- Laflamme E M, Linder E, Pan Y B. 2016. Statistical downscaling of regional climate model output to achieve projections of precipitation extremes. *Weather Clim Extremes*, 12: 15–23
- Le Roux R, Katurji M, Zawar-Reza P, Quénol H, Sturman A. 2018. Comparison of statistical and dynamical downscaling results from the WRF model. *Environ Model Softw*, 100: 67–73
- Li H K, Lei Y C. 2010. Evaluation of Forest Biomass and Carbon Storage in China (in Chinese). Beijing: China Forestry Publishing House
- Li J, Heap A D. 2014. Spatial interpolation methods applied in the environmental sciences: A review. *Environ Model Softw*, 53: 173–189
- Li K, Jackson A, Livermore P W. 2014. Variational data assimilation for a forced, inertia-free magnetohydrodynamic dynamo model. *Geophys J Int*, 199: 1662–1676
- Li Z L. 2007. *Algorithmic Foundation of Multi-Scale Spatial Representation*. London: CRC Press
- Magnussen S, Næsset E, Wulder M A. 2007. Efficient multiresolution spatial predictions for large data arrays. *Remote Sens Environ*, 109: 451–463
- Mann H B. 1945. Nonparametric tests against trend. *Econometrica*, 13: 245–259
- Maude A D. 1973. Interpolation—Mainly for graph plotters. *Comput J*, 16: 64–65
- Misaghian N, Assareh M, Sadeghi M T. 2018. An upscaling approach using adaptive multi-resolution upgridding and automated relative permeability adjustment. *Comput Geosci*, 22: 261–282
- Mitchell M N B. 2012. *Data fusion: Concepts and Ideas*. Berlin: Springer-Verlag
- National Bureau of Statistics of China. 2018. *China Statistical Yearbook*. Beijing: China Statistics Press
- Nichols N K. 2010. Mathematical concepts of data assimilation. In: Lahoz W, Khattatov B, Menard R, eds. *Data Assimilation: Making Sense of Observations*. Berlin: Springer. 13–39
- Peng C H, Guiot J, Wu H B, Jiang H, Luo Y Q. 2011. Integrating models with data in ecology and palaeoecology: Advances towards a model-data fusion approach. *Ecol Lett*, 14: 522–536
- Phillips J D. 2002. Global and local factors in earth surface systems. *Ecol Model*, 149: 257–272
- Ponsar S, Luyten P, Dulière V. 2016. Data assimilation with the ensemble Kalman filter in a numerical model of the North Sea. *Ocean Dyn*, 66: 955–971
- Schneider B. 2001. Phenomenon-based specification of the digital representation of terrain surfaces. *Trans GIS*, 5: 39–52
- Schoenberg I J. 1946. Contributions to the problem of approximation of equidistant data by analytic functions. *Quar Appl Math*, 4: 45–99, 112–141
- Seppelt R, Lautenbach S, Volk M. 2013. Identifying trade-offs between ecosystem services, land use, and biodiversity: A plea for combining scenario analysis and optimization on different spatial scales. *Curr Opin Env Sust*, 5: 458–463
- Shepard D. 1968. A two-dimensional interpolation function for irregularly-spaced data. In: Proceedings of the 1968 23rd ACM National Conference. New York: Association for Computing Machinery
- Shi W J, Yue T X, Fan Z M. 2011. An overview of high accuracy surface modeling of soil properties. *Procedia Environ Sci*, 13: 2304–2309
- Shi W, Liu J, Du Z, Song Y, Chen C, Yue T. 2009. Surface modelling of soil pH. *Geoderma*, 150: 113–119
- Smith B, Prentice I C, Sykes M T. 2001. Representation of vegetation dynamics in the modelling of terrestrial ecosystems: Comparing two contrasting approaches within European climate space. *Glob Ecol Biogeogr*, 10: 621–637
- Smith B, Wårlind D, Arneth A, Hickler T, Leadley P, Siltberg J, Zaehle S. 2014. Implications of incorporating N cycling and N limitations on primary production in an individual-based dynamic vegetation model. *Biogeosciences*, 11: 2027–2054
- Somasundaram D. 2005. *Differential Geometry*. Harrow: Alpha Science International
- Spivak M. 1979. *A Comprehensive Introduction to Differential Geometry* (Vol. 3). Boston: Publish or Peril
- Talmi A, Gilat G. 1977. Method for smooth approximation of data. *J Comput Phys*, 23: 93–123
- Tse R O C, Gold C. 2004. TIN meets CAD—Extending the TIN concept in GIS. *Future Generation Comput Syst*, 20: 1171–1184
- Usery E L, McMaster R B. 2005. Introduction to the UCGIS research agenda. In: Usery E L, McMaster R B, eds. *A Research Agenda for Geographic Information Science*. London: CRC Press. 1–16
- Wang H W, Wang Y H. 2012. Analysis of spatial interpolation methods. In: Qian Z H, Cao L, Su W L, Wang T K, Yang H M, eds. *Recent Advances in Computer Science and Information Engineering (Lecture Notes in Electrical Engineering Vol. 129)*. Berlin: Springer. 507–512
- Yue T X, Ai N S. 1990. The mathematic model of cirque morphology. *J Glaciol Geocryol*, 12: 227–34
- Yue T X, Chen S P, Xu B, Liu Q S, Li H G, Liu G H, Ye Q H. 2002. A curve-theorem based approach for change detection and its application to Yellow River Delta. *Int J Remote Sens*, 23: 2283–2292
- Yue T X, Du Z P, Liu J Y. 2004. High accuracy surface modelling and its error analysis (in Chinese). *Prog Nat Sci*, 14: 300–306
- Yue T X, Du Z P, Song D J, Gong Y. 2007. A new method of surface modeling and its application to DEM construction. *Geomorphology*, 91: 161–172

- Yue T X, Song Y J. 2008. The YUE-HASM method. In: Li D, Ge Y, Foody G M, eds. Accuracy in Geomatics. Edgbaston: World Academic Union. 148–153
- Yue T X, Wang S H. 2010. Adjustment computation of HASM: A high-accuracy and high-speed method. *Int J Geogr Inf Sci*, 24: 1725–1743
- Yue T X, Chen C F, Li B L. 2010a. An adaptive method of high accuracy surface modeling and its application to simulating elevation surfaces. *Trans GIS*, 14: 615–630
- Yue T X, Song D J, Du Z P, Wang W. 2010b. High-accuracy surface modelling and its application to DEM generation. *Int J Remote Sens*, 31: 2205–2226
- Yue T X. 2011. Surface Modelling: High Accuracy and High Speed Methods. Boca Raton: CRC Press
- Yue T X, Chen C F, Li B L. 2012. A high-accuracy method for filling voids and its verification. *Int J Remote Sens*, 33: 2815–2830
- Yue T X, Zhao N, Yang H, Song Y J, Du Z P, Fan Z M, Song D J. 2013a. A multi-grid method of high accuracy surface modeling and its validation. *Trans GIS*, 17: 943–952
- Yue T X, Zhao N, Ramsey R D, Wang C L, Fan Z M, Chen C F, Lu Y M, Li B L. 2013b. Climate change trend in China, with improved accuracy. *Clim Change*, 120: 137–151
- Yue T X, Zhang L L, Zhao N, Zhao M W, Chen C F, Du Z P, Song D J, Fan Z M, Shi W J, Wang S H, Yan C Q, Li Q Q, Sun X F, Yang H, Wilson J, Xu B. 2015a. A review of recent developments in HASM. *Environ Earth Sci*, 74: 6541–6549
- Yue T X, Zhao M W, Zhang X Y. 2015b. A high-accuracy method for filling voids on remotely sensed XCO₂ surfaces and its verification. *J Cleaner Product*, 103: 819–827
- Yue T X, Du Z P, Lu M, Fan Z M, Wang C L, Tian Y Z, Xu B. 2015c. Surface modeling of ecosystem responses to climatic change in Poyang Lake Basin of China. *Ecol Model*, 306: 16–23
- Yue T X, Liu Y, Zhao M W, Du Z P, Zhao N. 2016a. A fundamental theorem of Earth's surface modelling. *Environ Earth Sci*, 75: 751
- Yue T X, Zhao N, Fan Z M, Li J, Chen C F, Lu Y M, Wang C L, Xu B, Wilson J. 2016b. CMIP5 Downscaling and its uncertainty in China. *Glob Planet Change*, 146: 30–37
- Yue T X, Wang Y F, Du Z P, Zhao M W, Li Zhang L, Zhao N, Lu M, Larocque G R, Wilson J P. 2016c. Analysing the uncertainty of estimating forest carbon stocks in China. *Biogeosciences*, 13: 3991–4004
- Zhang L L, Yue T X, Wilson J P, Zhao N, Zhao Y P, Du Z P, Liu Y. 2017a. A comparison of satellite observations with the XCO₂ surface obtained by fusing TCCON measurements and GEOS-Chem model outputs. *Sci Total Env*, 601–602: 1575–1590
- Zhao C Y, Nan Z G, Cheng G D. 2005. Methods for modelling of temporal and spatial distribution of air temperature at landscape scale in the southern Qilian mountains, China. *Ecol Model*, 189: 209–220
- Zhao M W, Zhang X Y, Yue T X, Wang C, Jiang L, Sun J L. 2017. A high-accuracy method for simulating the XCO₂ global distribution using GOSAT retrieval data. *Sci China Earth Sci*, 60: 143–155
- Zhao N, Yue T. 2014a. A modification of HASM for interpolating precipitation in China. *Theor Appl Climatol*, 116: 273–285
- Zhao N, Yue T X. 2014b. Sensitivity studies of a high accuracy surface modelling method. *Sci China Earth Sci*, 57: 1–11
- Zhao N, Yue T, Chen C, Zhao M, Du Z. 2018. An improved HASM method for dealing with large spatial data sets. *Sci China Earth Sci*, 61: 1078–1087
- Zhu A X. 2005. Research issues on uncertainty in geographic data and GIS-based analysis. In: Usery E L, McMaster R B, eds. A Research Agenda for Geographic Information Science. London: CRC Press. 197–223
- Zienkiewicz O C. 1967. The Finite Element Method in Structural and Continuum Mechanics. London: McGraw Hill

(Responsible editor: Xin LI)